ISSN 2693-0935

Ancient TL

Institute of Earth Surface Dynamics, University of Lausanne, 1015 Lausanne, Switzerland
http://ancienttl.org

December 2025, Volume 43, No. 2

Ancient TL

Started by the late David Zimmerman in 1977

Ancient TL

Short Communication

A note on count linearity in luminescence measurements using PMT modules

Sebastian Kreutzer[1]*, Dirk Mittelstraß[1,2]

[1]Institute of Geography, Heidelberg University, Germany
[2]Helmholtz Institute Freiberg for Resource Technology, Freiberg, Germany

*Corresponding author: sebastian.kreutzer@uni-heidelberg.de

Received: 19 August 2025; in final form: 24 October 2025; accepted: 24 October 2025

Abstract

Deviations from anticipated instrumental readings in luminescence measurements can result in systematic uncertainties that are challenging to quantify. In this study, we address the issue of count rate linearity of photomultiplier modules commonly employed in luminescence readers. Considering instrumental thresholds and typical signal outputs, in most scenarios, this deviation is not a concern. However, in corner cases where detectors are operated in regions where non-linearity of count rates becomes significant, corrections are necessary. This is a well-known issue, but to the best of our knowledge, not all measurement systems utilise a correction. In this note, we provide some technical background and show that the impact on the equivalent dose can reach easily 2 % even in conservative scenarios. We then demonstrate how this can be post-corrected using a straightforward dead-time non-linearity correction implemented in the R package 'Luminescence'.

Keywords: Luminescence, Signal detection, Dead-time linearity correction, Systematic uncertainty

1. Introduction

Shortly after Dirk started his PhD in Heidelberg, we engaged in a discussion over managing light output to avoid the photomultiplier tube (PMT) operating within its non-linear response range. The cardinal rule tells us, as it is with every technical component, that it should be operated well within specified performance limits. In our case, the PMT had documented linear response characteristics up to 6×10^6 cts s^{-1} but was cut-off by the reader at 3.5×10^6 cts s^{-1}. This appeared to be a pretty conservative safety margin, still, should we be worried? In the PMT datasheet, we found *count linearity* defined as the value at which *"[...] 10 % count loss"* is still acceptable (Hamamatsu, 2008b). Luminescence dating practitioners may not call it linear if those very count values are used for equivalent dose (D_e) calculation.

Dirk then pointed out that count value underestimation can easily reach ~ 2 % in case of $\sim 100,000$ counts per channel, for a resolution of 0.1 s per channel (e.g. 1×10^6 cts s^{-1}). Although such a count rate is likely perceived as a sufficiently bright signal by most practitioners, not causing sleepless nights, the difference did not seem negligible enough to be discarded. Hence, we used the correction formula already implemented in the R (R Core Team, 2025) package `'OSLdecomposition'` (Mittelstraß et al., 2022) and simulated corrected PMT response for counting modules typically encountered in our luminescence readers. The results (Fig. 1) and their potential implications for luminescence measurements got our attention.

The count value underestimation reaches 7.5 % at a count-rate of 1×10^6 cts s^{-1} for the Hamamatsu H7421-50, which is usually preferred for infrared-radiofluorescence (IR-RF) measurements. Even the UV-blue sensitive PMTs commonly used for OSL and TL dating exhibit a 1.8 % and 2.6 % underestimation at the same count-rate. Of course, PMT signal dead-time correction is not a new issue. For instance, the Risø OSL/TL reader manual dedicates an entire chapter to it and describes a correction procedure (see Ch. 5 in Risø DTU, 2021). In the BINX-file, the logical parameter `DTENABLED` would indicate whether a correction was used.

However, how does non-linearity of counts translate, if this were to be the aim of a measurement, to an equivalent dose (D_e)? Should we correct the signals or does the correc-

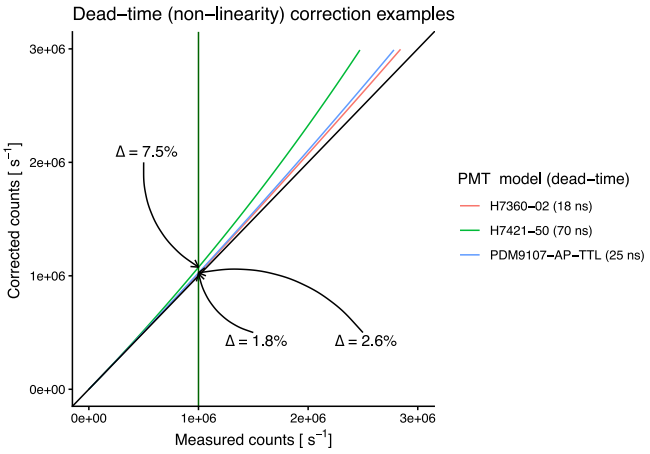

Figure 1: Examples for dead-time non-linearity corrected photon counts of different PMT models commonly installed in the luminescence readers. The cut-off shown by the vertical line was chosen arbitrarily to provide a reference for comparison. The Δ values show the expected deviation between measured and corrected value at the reference level.

tion introduce additional problems?

These questions are quite general and part of ongoing endeavours in our community to determine the origin, magnitude, and statistical significance of all kinds of measurement uncertainties (e.g., Galbraith, 2002; Duller, 2007; Li, 2007; Adamiec et al., 2012; Kreutzer et al., 2013; Zink, 2015; Bluszcz et al., 2015; Carter et al., 2018; Guérin et al., 2021). This is cumbersome and tedious work but often enough worth the effort if systematic uncertainties can be reduced or at least correctly expressed.

To fast forward, our discussion ended with adding a new function called `correct_PMTLinearity()` to `'Luminescence'` (Kreutzer et al., 2025) available with v1.1.1 (2025-09-11). In this contribution, we provide the technical background and discuss the potential impact on equivalent dose estimates. The succinct version for impatient readers: signal correction is likely to have an effect, but accurately quantifying its impact is challenging due to the number of involved parameters.

2. Technical background

In a PMT module, incoming light produces free electrons via the photoelectric effect. These electrons are then multiplied in a multi-staged high voltage field. If the PMT operates in photon-counting mode, these electron avalanches form current pulses that can be digitally counted. The number of counts is determined by the flux of photons with energies within the wavelength detection range of the PMT. The lower limit of the count rate is defined by the dark current, which represents an unavoidable signal background even in the absence of light input. It is caused by a thermally induced leakage current in the photocathode. The upper limit is reached when the system stops to differentiate individual pulses due to a high photon flux. This can result in either no output (paralysed mode) or in temporal or lasting blinding of the PMT (non-paralysed mode). The extent of the linear range depends on various factors, of which the pulse-pair resolution is the dominating one. The pulse-pair resolution is typically expressed in nanoseconds (10^{-9} s) and represents the shortest possible time span at which the system can distinguish individual pulses. If two pulses occur within this time span, the PMT will return only one count, thus underestimating the photon flux. The time span given by the pulse-pair resolution is also called detector dead-time.

As long as the count rate stays within the range of linearity, photon flux underestimation due to detector dead-times can be corrected using the formula

$$N = \frac{M}{1 - M\kappa} \tag{1}$$

where N (s^{-1}) is the true count rate, M (s^{-1}) the measured count rate, and κ (10^{-9} s) the pulse-pair resolution, respectively, the detector dead-time. For more details, we refer to the freely accessible photomultiplier handbook by Hamamatsu (Hamamatsu Photonics K.K., 2017), from which we drew also most of the technical background above.

This is all but news and frequently encountered statements regarding the count linearity of particular PMTs often include dead-time correction. However, it does not imply that this correction is automatically applied. For instance, the Freiberg Instruments lexsyg systems (Richter et al., 2025) do not automatically correct for PMT dead-time non-linearity but use detector overload thresholds that can be defined in the firmware settings[1] individually for each detector. The obvious idea is to avoid non-linear counting altogether or at least limit the effects. Nevertheless, depending on the PMT module operated at the margins of those limits, a correction might still be worth looking into it.

In Table 1 we list the PMTs most found in the systems operated in our community. The ET Q9235QB is a standard option available in, e.g., Risø (Bøtter-Jensen, 1997), lexsyg (Richter et al., 2025), Daybreak (Bortolot, 2000), and the LF02 (Baly et al., 2023) systems. The other detectors are either of newer design (e.g., ET PDM9107 series) or have different detection wavelengths for the red or infra-red range, and are probably less commonly installed in readers. Except for the ET Q9235QB PMT, pulse-pair-resolution data required for the linearity correction are part of the technical information provided along with the modules by the manufacturers. For the ET Q9235QB, it depends on the chosen housing, respectively the counting module, which may differ. Therefore, for this model we have quoted an assumed value. The linear detection range and κ vary between detectors causing different linearity corrections as exhibited in Fig. 1.

If we were to compare only single luminescence signals, such as two quartz thermoluminescence (TL) curves, disregarding other effects, the correction according to Eq. 1 is

[1] Line in the XML settings file:
`<cFIParameter Name="DetectorSelectorOverloadSettings" .../>`

Table 1: Specifications of selected photon-counting modules typically used in the luminescence-dating community.

Model	**Detection window [nm]**	**Manufacturer**	**10 % count loss [s^{-1}]**	**Pulse-pair resolution [ns]**	**Reference**
ET Q9235QB[(a)]	290–630	ET Enterprises	$> 10 \times 10^{6}$[(a)]	~ 25	ET Enterprise Ltd (2010)
PDM9107-AP-TTL PDM9107-USB	280–630	ET Enterprises	$\sim 3 \times 10^{6}$[(b)]	25	ET Enterprise Ltd (2017)
H7421-40[(c)]	320–720	Hamamatsu Photonics	$\sim 1.5 \times 10^{6}$	70	Hamamatsu (2008b)
H7421-50[(c)]	380–890	Hamamatsu Photonics	$\sim 1.5 \times 10^{6}$	70	Hamamatsu (2008b)
H7360-02[(d)]	300–650	Hamamatsu Photonics	6×10^{6}	18	Hamamatsu (2008a)

[(a)] Characteristics may differ with attached housing and counting module.
[(b)] After dead-time correction up to $100 \times 10^{6}\ s^{-1}$
[(c)] Model discontinued 12/2024, new series with comparable properties: H16721 (Hamamatsu, 2025)
[(d)] Model discontinued, suitable replacement with equal properties as above: H11870

straightforward, and the effect as shown in Fig. 1 is correctly quantified. However, typical measurement protocols used for D_e determination, such as the single-aliquot-regenerated (SAR) dose protocol (Murray and Wintle, 2000), involve more steps, and the physics of luminescence production (e.g., Bailey, 2001) does not provide a direct path to quantify the impact on the results. In other words, while Fig. 1 makes a compelling case, it is overly simplified because the effects in the D_e cannot be derived from single count values alone.

3. Simulation of equivalent dose impact

To simulate the ratio of D_e values determined with uncorrected and corrected signals, we simulated a SAR sequence using the R package `'RLumModel'` (v0.2.11) (Friedrich et al., 2016) and the Bailey (2001) quartz model. With an assumed dose rate of $1\,Gy\,s^{-1}$ for the irradiation source, we added regeneration dose points up to 1,000 Gy for each experiment to ensure a similar dose-response curve (DRC) shape. The unusual size of the dose rate (compared to typical $0.1\,Gy\,s^{-1}$ in built-in irradiation sources) does not affect the outcome of our experiment. We then modified the given dose to be recovered to move theoretical points along the set of DRCs. The D_e was derived from DRCs obtained for dead-time non-linearity-corrected and uncorrected shine-down curves. For the correction, we used a κ of 18 ns as the lowest value in Table 1. To simulate different light levels, we used a factor $(0.0001, 0.0002, \ldots, 0.001)$ to reduce the intensity of the shine-down curves. This was less challenging than modifying the Bailey-model to obtain realistic magnitudes of count values as typically measured with PMT modules. However, it resulted in non-meaningful dark-count values as such simulation is typically not part of the model implementation. The latter was still acceptable because the modelling output using differential equations does not include stochastic uncertainties (see discussion in Pagonis et al., 2020). With that being said, the chosen settings (light level and κ) are not entirely arbitrary but best align with the Hamamatsu H7360-02 PMT operated in most of our lexsyg readers here in Heidelberg.

Our modelling sequence was defined with the following parameters:

```
sequence <- list(
  RegDose = <dose_points>,
  TestDose = 25,
  PH = 220, #preheat
  CH = 220, #cutheat
  OSL_temp = 125, #read temp.
  Irr_2recover = <given_dose>,
  OSL_duration = 70)
```

This sequence was then used by `'RLumModel'` to simulate the corresponding DRC:

```
RLumModel::model_LuminescenceSignals(
  sequence = sequence,
  simulate_sample_history = TRUE,
  model = "Bailey2001",
  lab.dose_rate = 1,
  ...)
```

The full R script used for our simulation is attached as a supplement for detailed inspection. For this manuscript, Fig. 2 suffices and illustrates the basic concept of our simulation. For simplicity, we show only shine-down curves for one intensity setting, while the script produces a set of curves for each SAR sequence using different intensities for each particular dose to recover.

Figure 3 shows the output of our simulation. The primary x-axis and y-axis refer to the plotted but arbitrary values, while the secondary axes provide the conversion to physically meaningful quantities. For the x-axis, these are Gy and for the y-axis absolute signal intensity. This seems to contradict the given dose (primary x-axis), but indeed, with dose, the Bailey (2001) model-based simulated SAR protocol increasingly fails to recover the given dose; a model property unrelated to the applied dead-time correction. A similar pattern can be found for other quartz luminescence models that are included in `'RLumModel'`.

The colours in the heatmap encode the obtained ratio of the corrected and uncorrected D_e values. The white solid contour lines provide guidance to better connect colours with the scales on the axes. For ratios > 1 the D_e derived from corrected shine-down curves is higher. For ratios < 1 the

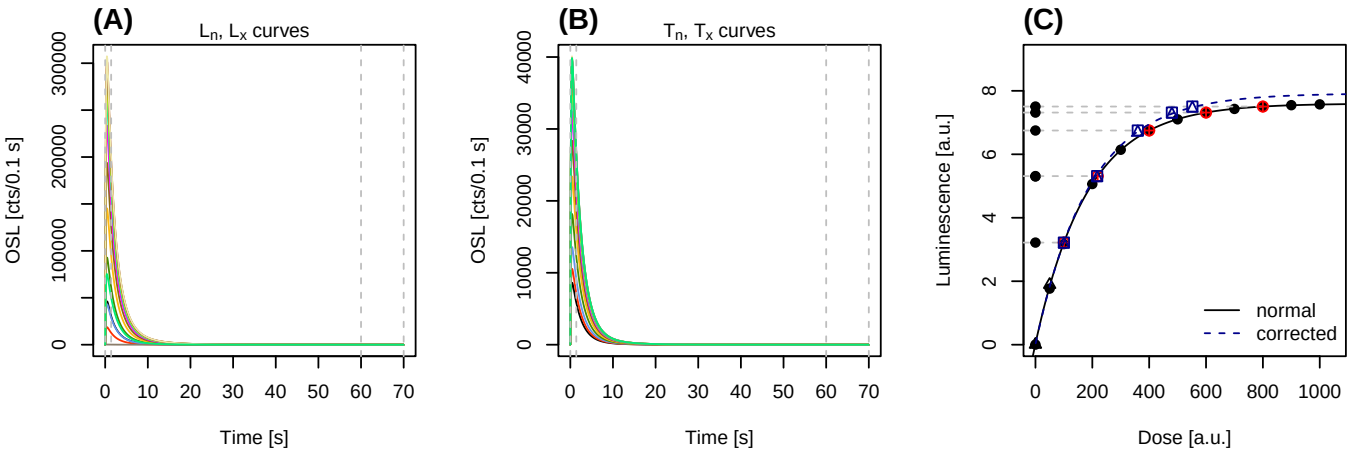

Figure 2: Typical simulated shine-down curves for L_x (A) and T_x (B) and the corresponding dose-response curve (C). In (C) we added the different L_n/T_n points for which different D_e values can be calculated either for the uncorrected signals (solid black line) or the DRC based on dead-time non-linearity corrected shine-down curves (dashed blue line). More details see main text.

corrected D_e is lower, which is the case for most simulated scenarios. This is because the correction of the shine-down curves causes less curvature of the DRC and the corresponding corrected D_e derived from such curves yields smaller values.

In our example, the calculated ratios between D_e values obtained with and D_e values obtained without correction, range from 0.92 to 1.01 in corner cases. Realistically, the difference between D_e values derived from uncorrected signals to D_e values based on dead-time non-linearity corrected signals will ballpark 1–2 %. For approximation, we assume that most quartz D_e values will be lower than 200 Gy in dating scenarios. Please note that ratios in Fig. 3 and as they may appear in Fig. 2 are not comparable, because the hypothetical DRC added as a dashed blue line in Fig. 2 would only exist for one scenario of a dose to be recovered.

During a SAR measurement, as simulated here, the light output can decrease or increase depending on the regeneration dose, preheat/cutheat temperatures, and sensitivity changes; all related to the process of luminescence production. SAR protocol tests, e.g., dose-recovery tests, and test dose measurements during the sequence should account and correct for this, given that light output readings are reliable and not affected by instrumental changes that are not part of underlying luminescence physics. Unfortunately, the number of parameters we can modify for this model and simulation alone is huge and the number of possible scenarios nearly infinite. Hence, the simulation demonstrates that instrumental aspects are better taken care of to avoid hard-to-quantify systematic uncertainties later.

4. When and how to apply linearity correction?

The simulation suggests small but non-negligible D_e overestimations, if samples with high signal yield are evaluated without PMT-linearity corrections. However, at what count values should we start to worry and look for a solution?

A simple marker is the first channel of the first OSL measurement (e.g., L_n in the SAR protocol). This data point is typically the one with the highest impact on the obtained D_e. In Table 2 we provide rule-of-thumb values to make an assessment of the situation. We calculated at which count value the count underestimation exceeds 1 % depending on the channel width and the employed PMT.

In cases, where non-linearity seems to become a concern, we have identified three possible solutions that can be applied; in parts combined.

1. **Monitor and manage light output:** The most effective method to prevent any potential issues is to adhere to the most straightforward principle: avoid operating detectors close to or beyond their specified count linearity. This can be achieved through various means, including increasing the detector to sample distance, reducing the stimulation intensity while prolonging the stimulation duration, or employing the most straightforward approach of adding neutral density filters. These filters can be as simple as home-made pin-hole filters. Altering the aliquot size for the sake of lower light output should be avoided, though.

2. **Record dead-time profiles:** The second-most effective solution appears to be the one outlined in the Risø handbook: Record a linearity profile (Risø DTU, 2021). If this is supported by the manufacturer, it gives complete control and establishes a distinct threshold above which signals should be discarded.

3. **Post-correction:** Once the signal has been recorded but a linearity profile has not been established for the detector, post-processing using the linearity correction routine becomes appropriate. In the `'Luminescence'` package, we have integrated the function `correct_PMTLinearity()` as part of this contribution. The user can provide `RLum.Analysis-class` or `RLum.Data.Curve-class` objects as input, specify the

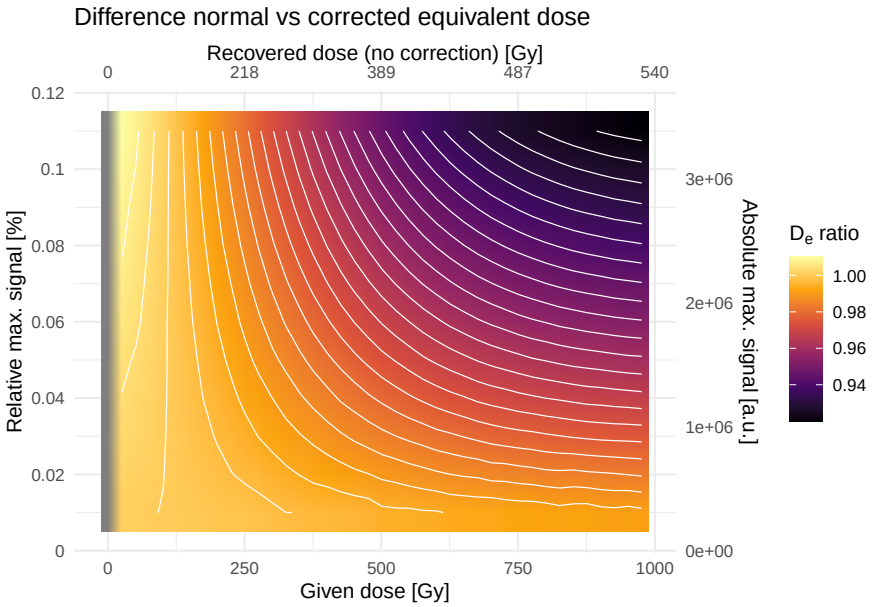

Figure 3: Simulated effect of signal strength and given dose on the difference of equivalent doses between the uncorrected and corrected signal. The secondary x and y-axes provide supplementary information on the recovered dose (x-axis) using the simulation for a specific given dose, and the expected absolute count value (y-axis), for which the unit can be assumed as cts s^{-1}. Please note that the numerical values depend on the model parameters of the simulation, and the graph serves solely as an indication of the anticipated impact. For further details, we refer to the main text.

Table 2: Counts per channel (CH) with an estimated difference of 1 % between measured and corrected value.

Pulse-pair-resolution	**CH = 0.05 s**	**CH = 0.1 s**	**CH = 0.2 s**	**CH = 0.5 s**	**CH = 1 s**	**PMT examples**
18 ns	27 778	55 556	111 111	277 778	555 556	H7360/H11870 series
25 ns	20 000	40 000	80 000	200 000	400 000	ET Q9235QB, PDM9107-APTTL series
70 ns	7 143	14 286	28 571	71 429	142 857	H7421/H16721 series

count-pair resolution, and then correction is performed automatically. If the input is an `.xsyg` file produced by a lexsyg reader, a new argument available through `import_Data(..., auto_linearity_correction = TRUE)` (through `read_XSYG2R()`) will attempt an automatic correction using count-pair resolution values for known detectors. However, while convenient, the automatic correction remains patchy, as not all versions of *LexStudio2* (the operating software for lexsyg readers) return information on the detector. In such cases, the manual call on `correct_PMTLinearity()` is the more reliable approach.

Solution 1 can be combined with either solution 2 or solution 3. In cases were dead-time profiles were established, no post-procession correction (solution 3) must be applied.

Finally, it should be noted that any solution relies on the non-paralysed operation mode of the PMT. If the PMT becomes dark in response to temporal overloads, the dead-time non-linearity correction will not be effective. On the other hand, a post-correction might be beneficial even in cases where only a fractional non-linearity might be expected to avoid systematic deviations and errors.

5. Conclusion and outlook

We discussed the well-known issue of non-linear counting of PMT modules commonly utilized for measuring luminescence. Our attempt to quantify the impact on the equivalent dose in SAR measurements would estimate a systematic uncertainty of up to 2 % for quartz OSL measurements even when using PMTs with a high pulse-pair resolution of 18 ns.

We propose managing the light output to mitigate such effects or recording linearity profiles. Alternatively, if this approach is not feasible, we suggest post-correcting luminescence signals using the new function `correct_PMTLinearity()` added to `'Luminescence'`.

Our results are based on simulations with the objective of ensuring reproducibility and adaptation by others. Future work may necessitate re-analysing previously measured data to quantify the effect on the age and chronological inference for luminescence dating measurements.

Data availability. The R script used to generate the modeling results is available as Supplementary Material to this article.

Conflict of interest. SK is a member of the Editorial Board of Ancient TL.

Financial support. SK acknowledges funding through the DFG Heisenberg programme (#505822867), DM through the DFG project ARENICOLA (#553815036).

Review. This article was reviewed by an anonymous reviewer.

References

Adamiec, G., Heer, A.J., Bluszcz, A., 2012. Statistics of count numbers from a photomultiplier tube and its implications for error estimation. Radiation Measurements 47, 746–751. doi: 10.1016/j.radmeas.2011.12.009.

Bailey, R.M., 2001. Towards a general kinetic model for optically and thermally stimulated luminescence of quartz. Radiation Measurements 33, 17–45. doi: 10.1016/s1350-4487(00)00100-1.

Baly, L., Arteche, R., van Espen, P., Arteche, J., Quesada, I., García, M., Lubián, H., Cepero, T., Baly, M., Gutiérrez, J.C., Chávez, A., Valle, R.A.D., Hernández, L.P., 2023. The LF02 automated luminescence reader. Ancient TL 41, 6–13. doi: 10.26034/la.atl.2023.571.

Bluszcz, A., Adamiec, G., Heer, A.J., 2015. Estimation of equivalent dose and its uncertainty in the OSL SAR protocol when count numbers do not follow a Poisson distribution. Radiation Measurements 81, 46–54. doi: 10.1016/j.radmeas.2015.01.004.

Bortolot, V.J., 2000. A new modular high capacity OSL reader system. Radiation Measurements 32, 751–757. doi: 10.1016/s1350-4487(00)00038-x.

Bøtter-Jensen, L., 1997. Luminescence techniques: Instrumentation and methods. Radiation Measurements 27, 749–768. doi: 10.1016/S1350-4487(97)00206-0.

Carter, J., Cresswell, A., Kinnaird, T., Carmichael, L., Murphy, S., Sanderson, D., 2018. Non-Poisson variations in photomultipliers and implications for luminescence dating. Radiation Measurements 120, 267–273. doi: 10.1016/j.radmeas.2018.05.010.

Duller, G.A.T., 2007. Assessing the error on equivalent dose estimates derived from single aliquot regenerative dose measurements. Ancient TL 25, 15–24. doi: 10.26034/la.atl.2007.403.

ET Enterprise Ltd, 2010. 51 mm (2") photomultiplier: 9235B series data sheet. Datasheet. Uxbridge, GB. URL: `https://et-enterprises.com/images/data_sheets/9235B.pdf`.

ET Enterprise Ltd, 2017. Photodetector module - PDM TTL series data sheet. Datasheet. Uxbridge, GB. URL: `https://et-enterprises.com/images/data_sheets/PDM_TTL_Series.pdf`.

Friedrich, J., Kreutzer, S., Schmidt, C., 2016. Solving ordinary differential equations to understand luminescence: 'RLumModel' an advanced research tool for simulating luminescence in quartz using R. Quaternary Geochronology 35, 88–100. doi: 10.1016/j.quageo.2016.05.004.

Galbraith, R.F., 2002. A note on the variance of a background-corrected OSL count. Ancient TL 20, 49–51. doi: 10.26034/la.atl.2002.348.

Guérin, G., Lahaye, C., Heydari, M., Autzen, M., Buylaert, J.P., Guibert, P., Jain, M., Kreutzer, S., Lebrun, B., Murray, A.S., Thomsen, K.J., Urbanova, P., Philippe, A., 2021. Towards an improvement of optically stimulated luminescence (OSL) age uncertainties: modelling OSL ages with systematic errors, stratigraphic constraints and radiocarbon ages using the R package BayLum. Geochronology 3, 229–245. doi: 10.5194/gchron-3-229-2021.

Hamamatsu, 2008a. Photon Counting Head: H7360-02. Datasheet.

Hamamatsu, 2008b. Photon Counting Head: H7421-50 (40). Datasheet.

Hamamatsu, 2025. Discontinued products | Hamamatsu Photonics. URL: `https://www.hamamatsu.com/eu/en/support/discontinued-products.html`.

Hamamatsu Photonics K.K., 2017. Photomultiplier Tubes: Basics and Applications. 4th ed., Hamamatsu. URL: `https://www.hamamatsu.com.cn/content/dam/hamamatsu-photonics/sites/documents/99_SALES_LIBRARY/etd/PMT_handbook_v4E.pdf`.

Kreutzer, S., Burow, C., Dietze, M., Fuchs, M.C., Schmidt, C., Fischer, M., Friedrich, J., Mercier, N., Philippe, A., Riedesel, S., Autzen, M., Mittelstrass, D., Gray, H.J., Galharret, J.M., Colombo, M., Steinbuch, L., de Boer, A.M., 2025. Luminescence: Comprehensive luminescence dating data analysis. URL: `10.32614/CRAN.package.Luminescence`.

Kreutzer, S., Hülle, D., Thomsen, K.J., Hilgers, A., Kadereit, A., Fuchs, M., 2013. Quantification of cross-bleaching during infrared (IR) light stimulation. Ancient TL 31, 1–10. doi: 10.26034/la.atl.2013.468.

Li, B., 2007. A note on estimating the error when subtracting background counts from weak OSL signals. Ancient TL 25, 9–14. doi: 10.26034/la.atl.2007.402.

Mittelstraß, D., Kreutzer, S., Schmidt, C., 2022. OSLdecomposition: Signal component analysis for optically stimulated luminescence. URL: `https://doi.org/10.32614/CRAN.package.OSLdecomposition`.

Murray, A.S., Wintle, A.G., 2000. Luminescence dating of quartz using an improved single-aliquot regenerative-dose protocol. Radiation Measurements 32, 57–73. doi: 10.1016/s1350-4487(99)00253-x.

Pagonis, V., Kreutzer, S., Duncan, A.R., Rajovic, E., Laag, C., Schmidt, C., 2020. On the stochastic uncertainties of thermally and optically stimulated luminescence signals: A Monte Carlo approach. Journal of Luminescence 219, 116945. doi: 10.1016/j.jlumin.2019.116945.

R Core Team, 2025. Writing R Extensions: for R, version 4.5.1 (2025-06-13). URL: `https://cran.r-project.org/doc/manuals/R-exts.html`.

Richter, D., Richter, A., Kumar, T., Pintaske, R., Dornich, K., 2025. Lexsyg luminescence measurement devices: Status and outlook. Radiation Measurements 181, 107377. doi: 10.1016/j.radmeas.2025.107377.

Risø DTU, 2021. Guide to the Risø TL/OSL Reader. URL: `https://luminescence.dk/docs/Reader.pdf`.

Zink, A.J.C., 2015. Bayesian analysis of luminescence measurements. Radiation Measurements 81, 71–77. doi: 10.1016/j.radmeas.2015.04.009.

Ancient TL

Short Communication

Evaluating short-term post-irradiation instability of radiation-induced ESR signals in quartz

Eslem Ben Arous[1,2,3*], María Jesús Alonso Escarza[1], Verónica Guilarte[4], Sumiko Tsukamoto[5,6], Mathieu Duval[1,7,8]

[1]Centro Nacional de Investigación sobre la Evolución Humana (CENIEH), Burgos, Spain
[2]Human Palaeosystems Group, Max Planck Institute of Geoanthropology (MPI-GEA), Jena, Germany
[3]Histoire Naturelle des Humanités Préhistoriques (HNHP), CNRS–Université de Perpignan Via Domitia (UPVD)–Muséum national d'Histoire naturelle (MNHN), Paris, France
[4]Department of Science Education, University of Granada, Melilla, Spain
[5]LIAG-Institute for Applied Geophysics, Hannover, Germany
[6]Department of Geosciences, University of Tübingen, Tübingen, Germany
[7]Australian Research Centre for Human Evolution (ARCHE), Griffith University, Brisbane, Queensland, Australia
[8]Palaeoscience Labs, Department of Archaeology and History, La Trobe University Melbourne Campus, Bundoora, Victoria, Australia

*Corresponding author: ben-arous@gea.mpg.de

Received: 03 October 2025; in final form: 26 November 2025; accepted: 26 November 2025

Abstract

This study investigates the potential short-term fading of radiation-induced Electron Spin Resonance (ESR) signals in quartz grains following gamma-irradiation, a critical issue for the optimization of Single Aliquot (SA) measurement protocols. Through a signal stability experiment carried out on two quartz samples, we evaluated the evolution of the Al and Ti ESR signal intensities over 2 to 8 months after gamma irradiation. Our results indicate that the variation of the ESR intensities remains within typical experimental uncertainties, although data might also suggest a potential trend during the first day after irradiation. This trend is, however, non-systematic and could be sample- and signal-dependent, if not directly related to the stability of the experimental setup. Regardless, for precaution we may nevertheless recommend waiting for 1 day after gamma-irradiation before carrying out the ESR measurements. Importantly, this finding implies that ESR measurements of quartz samples can be performed relatively soon after gamma-irradiation, enabling the implementation of more time-efficient SAR protocols for ESR dating applications.

Keywords: Fading, ESR signal, Quartz, MAAD, SAR

1. Introduction

Most Multiple Centre Electron Spin Resonance (MC-ESR) dating studies based on sedimentary quartz grains typically use the standard Multiple Aliquot Additive Dose (MAAD) method for dose determination (e.g. Ben Arous et al., 2025, 2024b; Duval et al., 2017; Liu et al., 2010; Voinchet et al., 2020; Yokoyama et al., 1985). More convenient in many aspects than Single Aliquot (SA) procedures, especially when direct access to an irradiation source may be complicated, the MAAD method has demonstrably proven its reliability to constrain the chronology of Quaternary deposits in Europe, Asia, and Africa, providing results in good agreement with independent age control (e.g., Bartz et al., 2018, 2019; Ben Arous et al., 2024b, 2025; Duval et al., 2022; Voinchet et al., 2020). However, one may reasonably argue that ESR dose evaluations involving Single Aliquot and/or Regeneration procedures (e.g., SAR,

SAAD, MAR) show indisputable advantages compared to the MAAD method. For example, SA measurements require a significantly smaller amount of prepared material, which may be critical in quartz-poor deposits. In combination with Regeneration (SAR), it also involves significantly less irradiation dose steps, significantly reducing irradiation and measurement times. Typically, only 3–4 dose points may be needed for the dose response curve, compared to 10–12 dose points usually measured for the MAAD. Moreover, the dose evaluation based on SAR or MAR methods intrinsically offers a smaller fitting uncertainty, since the D_e is obtained by interpolation instead of back extrapolation. This is why the SAR has become an increasingly popular method in ESR dating over the last decade (e.g., Tsukamoto et al., 2015).

Time constraint being the essence of any experimental work, one of the main issues with regenerative dose measurement procedures is to properly evaluate whether any transient (short-lived) ESR signal induced by the irradiation may potentially interfere with the main radiation-induced ESR signals being measured for dating purposes. Such evaluation is crucial in order to determine the appropriate waiting time needed between the irradiation and subsequent ESR measurement. However, unlike for tooth enamel (e.g., Hoffmann and Mangini, 2002; IAEA, 2002; Nilsson et al., 2001; Sholom and Chumak, 2008), the possible presence of transient radiation-induced ESR signals in quartz grains remains virtually unknown to our knowledge.

Regardless of the above, two main conservative strategies have been traditionally adopted in ESR dating of quartz to mitigate the potential impact of transient signals on dose evaluation: (i) either a prolonged storage (which can vary from a few days to a few months depending on the material or laboratory involved) of the sample at room temperature (e.g. Fattibene and Callens, 2010), (ii) a post-irradiation annealing at a given temperature, regarded as sufficient to eliminate the temporary signals without affecting the radiation-induced signal of interest. This first one is usually favoured in dating application studies based on the MAAD method, and a minimum storage of a few weeks (the exact duration is very rarely reported) is commonly considered for extra precaution (e.g. Niu et al., 2022), although there is currently no published evidence that could possibly confirm, or invalidate, the need of such procedure. The second is usually preferred for SAR protocol measurement based on quartz (e.g. Tsukamoto et al., 2015). In simplified terms, to determine the equivalent dose with the SAR protocol, the natural ESR signal of a single aliquot is first measured after preheating at a specific temperature (typically between 120 °C and 280 °C for 2 min). This is followed by a high-temperature annealing step (420 °C for 2 min), irradiation with an X-ray source (given dose), another preheating step, and finally measurement of the regenerated ESR signal from the same aliquot. The ESR-SAR protocol offers the major advantage of saving considerable time, as it allows the quartz sample to be measured just a few minutes after irradiation and heating, unlike the MAAD protocol, where all irradiations are performed in a separate facility using a high dose rate source.

Consequently, the present study aims to evaluate the possible presence of transient radiation-induced ESR signals generated by gamma-irradiation, through a short-term stability experiment involving two quartz samples repeatedly measured over 2 and 8 months after irradiation. Such experiment is also crucial for the future implementation of the SAR protocol using gamma-irradiation sources.

2. Materials and methods

Two prepared quartz samples (100–200 µm grain size), OUC1102 and BG03-06, were selected for our experiment carried out at CENIEH (Spain). OUC1102 is a modern sample originating from the river bank of Oued Charef, Morocco (Ben Arous et al., 2024a; Sala-Ramos et al., 2022). BG03-06 was collected from the Middle Stone Age of Bargny 3 in Senegal (Ben Arous et al., 2024b). One natural aliquot of each sample (OUC1102: 304.6 mg; BG03-06: 150.9 mg) was irradiated with a Gammacell-1000 ^{137}Cs gamma-source (OUC1102: 1327 Gy; BG03-06: 1000 Gy) and then measured by ESR. Low temperature (90–92 K) ESR measurements were performed with an EMXmicro 6/1Bruker X-band ESR spectrometer coupled to a standard rectangular ER 4102ST cavity and using an ER4141VT digital temperature control unit. To ensure constant experimental conditions over time, the temperature of the water circulating in the magnet was controlled and stabilized at 18 °C by a water-cooled Thermo Scientific NESLAB ThermoFlex 3500 chiller, and the temperature of the room was kept constant at 20 °C by an air conditioning unit. Further details about the setup and its stability over time can be found in Duval and Guilarte Moreno (2012) and Guilarte and Duval (2020).

The ESR signals of both the Al and Ti centres were measured separately using the following acquisition parameters:

- Al centre: 10 mW microwave power, 1024 points resolution, 20 mT sweep width, 100 kHz modulation frequency, 0.1 mT modulation amplitude, 40 ms conversion time, 10 ms time constant and 1 scan.
- Ti centres: 5 mW microwave power, 1024 points resolution, 20 mT sweep width, 100 kHz modulation frequency, 0.1 mT modulation amplitude, 60 ms conversion time,10 ms time constant and 1 to 3 scans.

Each aliquot of a given sample was measured 3 times after a $\sim 120\,^{\circ}$ rotation in the cavity for both Al and Ti signals in order to consider angular dependence of the signal due to sample heterogeneity, and a mean value and an associated standard deviation were derived. Another quartz sample was used as a standard and measured immediately before and after the aliquots to evaluate the stability of the experimental conditions over time. Repeated ESR measurements of each aliquot together with the standard were carried out over a period of 8 months after after gamma-irradiation for OUC1102, and over 2 months for BG03-06.

The ESR intensity of the Al signal was extracted from peak-to-peak amplitude measurements between the top of the

first peak and the bottom of the last peak in the domain ranging from $g = 2.0185$ to $g = 1.9928$ (Toyoda and Falguères, 2003). The ESR intensity of the Ti centres was evaluated by peak-to-baseline amplitude measurement around $g = 1.913$ to $g = 1.915$ (i.e., options C and D sensu Duval and Guilarte, 2015). All ESR intensities were corrected for the slight variations of temperature (up to ~ 0.2 K) following Duval and Guilarte Moreno (2012), and of the overall stability of the experimental setup using the values from the quartz standard as a reference.

3. Results

The results obtained for the two samples and for each signal (Al, Ti-H and Ti-mix) are summarised in Table 1 and Fig. 1, while the numerical data may be found in Supplementary Material Tables S1 and S2.

An apparent trend may be observed in the ESR intensity of the Al signal of OUC1102 during the first 5 hours (300 min; Fig. 1B), which decreases by about 5 % from 5.57 to 5.30 a.u. Then, the values increase again and oscillate between 5.34 and 5.67 a.u. (Fig. 1A). In contrast, the Al signal intensity of BG03-06 first drops by about 4 % from 2.11 to 2.02 a.u., and then shows a slight but constant increase during the first 5 hours of about 11 % (from 2.02 to 2.25 a.u.) (Fig. 1D). This trend seems to disappear after 1 day, and ESR intensities remain overall constant between 1.96 and 2.14 a.u. (Fig. 1C).

Unlike the Al signal, the Ti signals measured in OUC1102 do not show any obvious apparent trend during the first 5 hours or beyond (Fig. 1E and F). In contrast, the two Ti signals of BG03-06 do show a similar notable increase over the first 5 hours of about 21 % (Ti-H; from 0.23 to 0.28 a.u.) and 18 % (Ti-mix; from 0.33 to 0.39 a.u.) (Fig. 1G and H). After 1 day, the ESR intensities seem to show instead a more random variation (Ti-H : 0.24–0.28 a.u.; Ti-mix: 0.32–0.37 a.u) and no significant trend may be observed. Interestingly, the evolution of the Al and Ti signals of BG03-06 is similar, although the overall variability of the Al is lower than that of the Ti signals.

Despite the variability observed in the Al and Ti signal intensities, both samples show that the mean intensity value remains virtually unchanged regardless of the time range considered. For OUC1102, the mean ESR intensities of the Al signal are between 5.51 ± 0.10 a.u. (234 days) and 5.44 ± 0.09 a.u. (1 day) and remain systematically consistent within uncertainty (Table 1). Similarly, the mean ESR intensities of the Ti-H and Ti-mix in that sample remain around 0.19 a.u. and 0.28–0.29 a.u., respectively (Table 1). BG03-06 also show mean ESR intensities varying within narrow range between 2.09 ± 0.06 a.u. (64 days) and 2.13 ± 0.06 a.u. (21 days), $\sim$0.26–0.27 a.u. and $\sim$0.34–0.35 a.u. for the Al, Ti-H and Ti-mix signals, respectively (Table 1). In other words, despite the variability observed, no significant difference in the ESR intensities of the various signals can be observed 2 hours, 1 day, 7 days and 14 days after gamma-irradiation when compared to the baseline values collected over a longer period (234 days for OUC1102 and 64 days for BG03-06).

This variability most likely originates from the inherent uncertainty associated with the stability of the experimental setup (about 1.1 % and 2.8 % for the Al and Ti signals; Duval et al., 2024; Duval and Guilarte Moreno, 2012) or with sample homogeneity, and especially the angular dependence of the signal. The latter is typically about 1.1 %, 2.0 % and 3.0 % for the Al, Ti-mix and T-H signals, although higher values may also be observed (Duval et al., 2024). Moreover, the variability is also strongly dependent on the signal-to-noise (S/N) ratio associated to each signal. For example, for sample BG03-06 the mean S/N ratio of the Al signal is about 2.1 and 5.4 times higher than that of the Ti-H and Ti-mix signals, respectively (Table 1). A similar observation can be made for sample OUC1102, with the Al signal showing an S/N ratio approximately 5–16 times higher on average for the various successive measurements (Table 1). Interestingly, with significantly stronger ESR intensities, the Al signal naturally tends to return a higher measurement precision compared to the Ti-mix and Ti-H signal (Duval et al., 2024). The same applies here. For example, at t = 6.89 days after irradiation, the Al, Ti-mix and Ti-H signal intensities show a scatter of 1.9 %, 3.1 % and 4.6 %, respectively (Table 1). For BG03-06, at t = 7.02 days, this variability is 2.9 % for the Al signal, while it is 5.3–5.4 % for both Ti signals. Importantly, these values are similar to those typically reported about the stability of the experimental setup (Duval et al., 2024; Duval and Guilarte Moreno, 2012).

Fig. 2 displays the spectra of the Al and Ti signals acquired at measurements #3, #33 and #63 for sample BG03-06. The Al spectra show little variability, with a slight shift of less than 1 Gauss (G) in the position of the first peak. A comparison of the ESR spectra obtained 7 days after gamma-irradiation with those acquired immediately after irradiation shows no significant differences for either Al or Ti signals. The small variations in peak intensity observed for Ti-mix or Ti-H are mostly attributable to high-frequency background noise, which is expected given the smaller S/N measured for these signals compared to Al. It is worth noting that other studies have reported changes in signal shape between spectra recorded immediately after irradiation and after preheating (e.g., Prince et al., 2024). However, such effects were not observed in our experiments, as the samples were not preheated. A slight difference in peak amplitude was observed, for example around 3500 G and 3525 G, which we initially attributed to the angular dependence of the signal. Nevertheless, as highlighted in Fig. 2 for measurement #63, the Ti-mix (signal D) exhibits a higher ESR intensity around 3525 G, while the Ti-H signal remains unchanged. This suggests that the observed variation is more likely related to the Ti-Li component rather than to angular dependence alone.

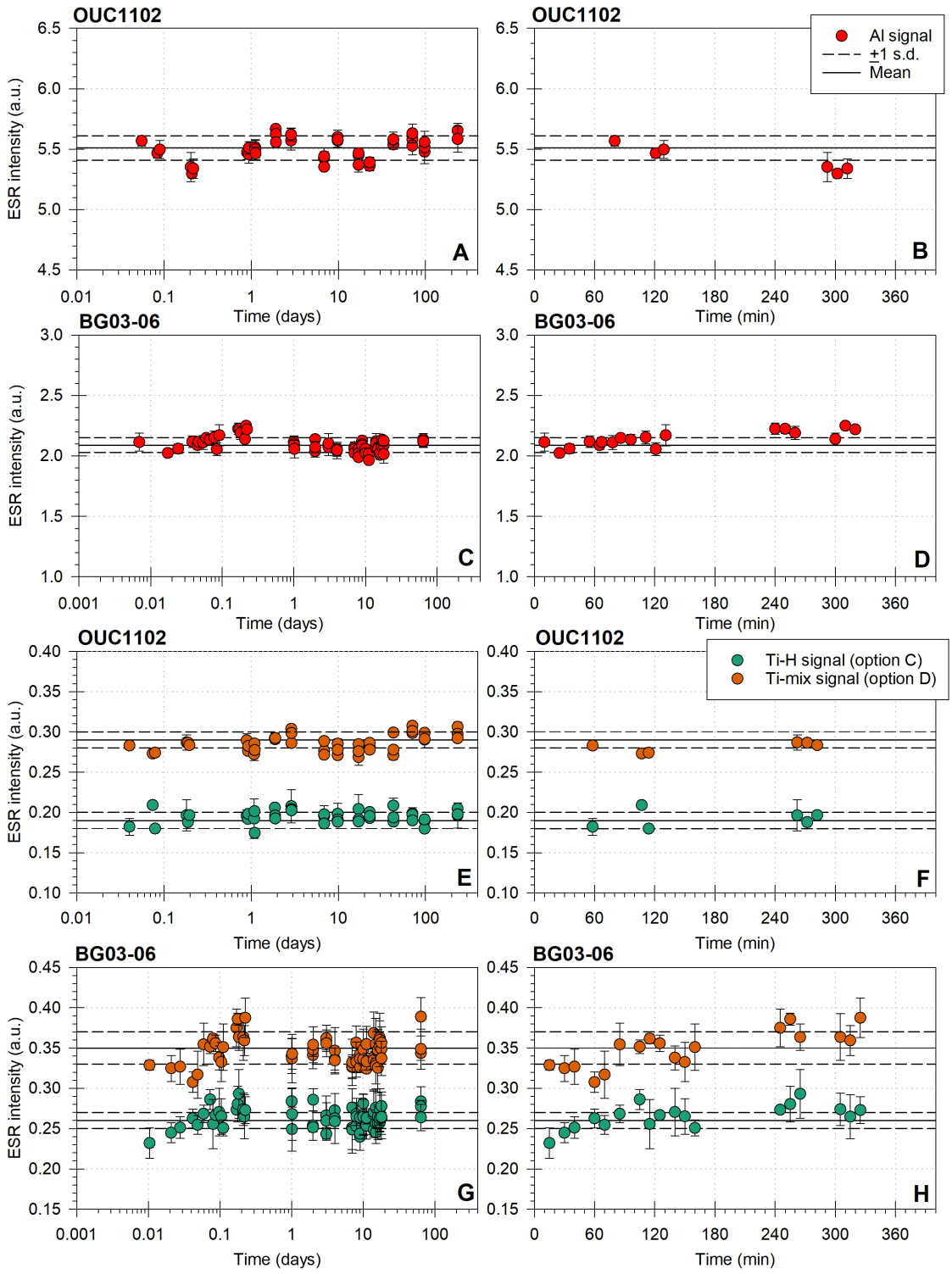

Figure 1: Evolution of the ESR intensities measured for the Al and Ti (options C and D sensu Duval and Guilarte, 2015) signals over almost 8 months (234 days) and 2 months (64 days) for samples OUC1102 and BG03-06, respectively. Left graphs (A, C, E, G) show the full evolution of the intensities over the full-time range. Right graphs (B, D, F, H) are focused on the first 400 minutes ($\sim$ 8 hours) after the irradiation. Graphs A to D show the Al signal, while graphs E to H display the Ti signals. Each point represents the mean ESR intensity and associated 1 standard deviation (s.d.) from the three measurements performed after a $\sim 120\,^{\circ}$ rotation. The mean ESR intensity (in arbitrary units – a.u.) and associated 1 sd over the full time range is also indicated by solid and dashed lines, respectively. All numerical values may be found in Supplementary Material Tables S1 and S2.

		Al signal			Ti-H signal option C sensu Duval and Guilarte (2015)			Ti-mix signal option D sensu Duval and Guilarte (2015)		
Sample	*n*	**Duration after irradiation [min/day]**	**Mean ESR intensity ± 1 sd (cv)**	**Average** S/N	**Duration after irradiation [min/day]**	**Mean ESR intensity ± 1 sd (cv)**	**Average** S/N	**Duration after irradiation [min/day]**	**Mean ESR intensity ± 1 sd (cv)**	**Average** S/N
OUC1102	3	129/0.09	5.51 ± 0.05 (1.7 %)	193	114/0.08	0.19 ± 0.02 (8.5 %)	12	114/0.08	0.28 ± 0.01 (2.0 %)	24
	9	1362/0.95	5.44 ± 0.09 (1.7 %)	145	1339/0.93	0.19 ± 0.01 (4.6 %)	15	1339/0.93	0.28 ± 0.01 (2.1 %)	28
	15	2775/1.93	5.49 ± 0.10 (1.8 %)	167	2728/1.89	0.19 ± 0.01 (4.8 %)	14	2728/1.89	0.28 ± 0.01 (2.5 %)	27
	21	9919/6.89	5.49 ± 0.10 (1.9 %)	163	9919/6.89	0.19 ± 0.01 (4.6 %)	14	9919/6.89	0.28 ± 0.01 (3.1 %)	29
	42	336889/234	5.51 ± 0.10 (1.7 %)	149	336913/234	0.19 ± 0.01 (4.0 %)	15	336913/234	0.29 ± 0.01 (3.6 %)	29
BG03-06	11	121/0.08	2.10 ± 0.04 (1.9 %)	45	125/0.09	0.26 ± 0.02 (6.0 %)	10	125/0.09	0.34 ± 0.02 (5.8 %)	12
	21	1460/1.01	2.13 ± 0.06 (2.9 %)	50	1465/1.02	0.27 ± 0.01 (5.6 %)	10	1465/1.02	0.35 ± 0.02 (6.1 %)	13
	33	10115/7.02	2.11 ± 0.06 (2.9 %)	42	10120/7.03	0.26 ± 0.01 (5.3 %)	14	10120/7.03	0.35 ± 0.02 (5.4 %)	17
	48	20175/14.01	2.09 ± 0.06 (3.0 %)	48	20230/14.05	0.26 ± 0.01 (4.5 %)	14	20230/14.05	0.34 ± 0.02 (4.9 %)	18
	63	92180/64.01	2.09 ± 0.06 (2.9 %)	54	92180/64.01	0.26 ± 0.01 (4.3 %)	15	92180/64.01	0.35 ± 0.02 (4.8 %)	20

Table 1: Mean ESR intensities and associated standard deviation measured for the Al, Ti-H (option C) and Ti-mix (option D) signals for a given duration, i.e., after about 2 hours, 1 day, 2 days, 1 week (7 days), and almost 8 months (234 days) for OUC1102, and after about 2 hours, 1 day, 1 week (7 days), 2 weeks (14 days) and about 2 months (64 days) for BG03-06. Key: n = measurement number; sd = standard deviation; cv = coefficient of variation. The average S/N (signal-to-noise ratio) has been calculated by averaging the noise at times 3, 9, 15, 21, 42 for sample OUC1102 and at times 11, 21, 33, 48 and 63 for sample BG03-06. All data, uncorrected and corrected with the standard are provided in the Supplementary Material.

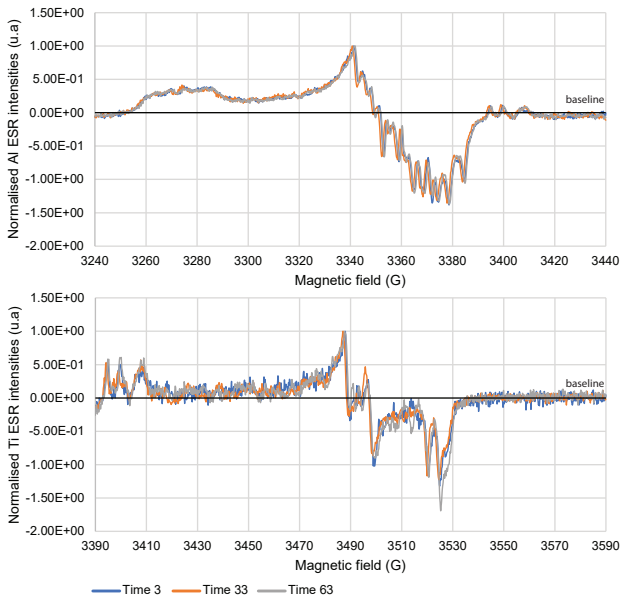

Figure 2: Comparison of normalised Al and Ti signals of sample BG03-06 from measurements #3, #33 and #63. A baseline correction using a cubic function was applied for each spectrum.

4. Summary

Our main observations may be summarised as follows:

- No apparent systematic trend in the short-term ESR signals stability is observed over time: while OUC1102 shows either a slight decrease (Al signal) or remains somewhat stable (Ti signals) during the first hours after gamma-irradiation, an intensity increase may instead be observed for all signals of BG03-06 over that same period.

- In other words, the more pronounced trends observed during the first day after gamma-irradiation are strongly signal- and sample-dependent. The intensity corrections performed using a standard measured together with the sample enable minimising the influence of the relative instability of the experimental setup on the data set, ensuring that the observed trends primarily reflect sample-specific behavior.

- Mean ESR intensities remain within error independently of the time range considered: over 2 hours, 1 day, 2 days or 7 seven days after gamma irradiation, the mean ESR intensity is consistent with the baseline value obtained over several months of measurements. This simply indicates that the ESR intensities measured shortly after gamma-irradiation do not significantly differ from the mean values derived from a longer time range.

5. Conclusions

Our results indicate that Al and Ti signals measured in two quartz samples do not exhibit on average any significant change in their intensity shortly (2 hours, 1 day, 2 days or even 7 days) after gamma-irradiation, suggesting that the transient radiation-induced signals, if present, have negligible influence on the measured ESR intensities. In other words, any potential transient signal generated immediately following the irradiation falls within the intrinsic experimental uncertainty, which is largely driven by factors such as the stability of the ESR spectrometer, the inherent heterogeneity of the quartz sample, or the S/N ratio. While some apparent trends may be punctually observed during the first 5 hours or 1 day after gamma-irradiation, they may be sample dependent and are possibly related to the stability of the ESR spectrometer, although the influence of the latter was tentatively minimised by repeatedly measuring a quartz standard. For precaution, it may nevertheless be recommended to wait at least 1 day after gamma-irradiation before performing the ESR measurements. An extension of the current study could involve preheating the gamma-irradiated samples followed by the same set of measurements.

Notably, our observations are consistent with those of Tsukamoto et al. (2015), who showed that Al and Ti centres remain stable over time following X-ray irradiation, with no significant differences between signals regenerated immediately after irradiation and those measured after one month of storage. Taken together, their findings and ours support the conclusion that potential short-lived components have little to no impact on ESR signal stability. As a corollary, these results also indicate that there is currently no evidence of short-term fading of the Al and Ti signals measured in quartz. As a consequence, this study provides an important experimental foundation for the future development and broader application of time-efficient Single Aliquot Regenerative dose (SAR) protocols using gamma-irradiation sources. Such advancement could significantly streamline the ESR dating workflow, particularly in contexts where sample quantity is limited or rapid turnaround is required.

Data availability. All data acquired in this study are available as Supplementary Material to this article.

Conflict of interest. The authors declare that they have no conflict of interest that could have biased their scientific work.

Financial support. EBA's postdoctoral research has received funding from the European Union's Horizon 2020 research and innovation programme under the Marie Skłodowska-Curie grant agreement No 101107408. MD's investigation is supported by the Spanish Ramón y Cajal Fellowship RYC2018-025221-I funded by MCIN/AEI/10.13039/501100011033 and by "ESF Investing in your future", and Grants PALEOMED PID2021-123092NB-C22 and GBCHRON PID2024-155126NB-I00, both funded by

MICIU/AEI/10.13039/501100011033 and by ERDF/EU.

Review. This article was reviewed by an anonymous reviewer.

References

Bartz, M., Arnold, L.J., Demuro, M., Duval, M., King, G.E., Rixhon, G., Álvarez Posada, C., Parés, J.M., Brückner, H., 2019. Single-grain TT-OSL dating results confirm an Early Pleistocene age for the lower Moulouya River deposits (NE Morocco). Quaternary Geochronology 49, 138–145. doi: 10.1016/J.QUAGEO.2018.04.007.

Bartz, M., Rixhon, G., Duval, M., King, G.E., Álvarez Posada, C., Parés, J.M., Brückner, H., 2018. Successful combination of electron spin resonance, luminescence and palaeomagnetic dating methods allows reconstruction of the Pleistocene evolution of the lower Moulouya river (NE Morocco). Quaternary Science Reviews 185, 153–171. doi: 10.1016/J.QUASCIREV.2017.11.008.

Ben Arous, E., Blinkhorn, J.A., Elliott, S., Kiahtipes, C., N'Zi, C., Bateman, M.D., Duval, M., Roberts, P., Patalano, R., Blackwood, A., Niang, K., Kouamé, E., Lebato, E., Hallett, E., Cerasoni, J.N., Scott, E., Lgner, J., Escarza, M.J.A., Guédé, F.Y., Scerri, E.M.L., 2025. Humans in Africa's wet tropical forests 150 thousand years ago. Nature 640, 402–407. doi: 10.1038/s41586-025-08613-y.

Ben Arous, E., Duttine, M., Duval, M., 2024a. How to measure the ESR intensity of the Al centre in optically bleached coarse quartz grains for dating purpose? Radiation Physics and Chemistry 214, 111307. doi: 10.1016/J.RADPHYSCHEM.2023.111307.

Ben Arous, E., Niang, K., Blinkhorn, J.A., Del Val, M., Medialdea, A., Coussot, C., Alonso Escarza, M.J., Bateman, M.D., Churruca Clemente, A., Blackwood, A.F., Iglesias-Cibanal, J., Saíz, C., Scerri, E.M.L., Duval, M., 2024b. Constraining the age of the Middle Stone Age locality of Bargny sites (Senegal) through a combined OSL-ESR dating approach. Quaternary Environments and Humans doi: 10.1016/j.qeh.2024.100044.

Duval, M., Arnold, L.J., Demuro, M., Parés, J.M., Campaña, I., Carbonell, E., Bermúdez de Castro, J.M., 2022. New chronological constraints for the lowermost stratigraphic unit of Atapuerca Gran Dolina (Burgos, N Spain). Quaternary Geochronology 71, 101292. doi: 10.1016/j.quageo.2022.101292.

Duval, M., Arnold, L.J., Guilarte, V., Demuro, M., Santonja, M., Pérez-González, A., 2017. Electron spin resonance dating of optically bleached quartz grains from the Middle Palaeolithic site of Cuesta de la Bajada (Spain) using the multiple centres approach. Quaternary Geochronology 37, 82–96. doi: 10.1016/j.quageo.2016.09.006.

Duval, M., Guilarte, V., 2015. ESR dosimetry of optically bleached quartz grains extracted from Plio-Quaternary sediment: Evaluating some key aspects of the ESR signals associated to the Ti-centers. Radiation Measurements 78, 28–41. doi: 10.1016/j.radmeas.2014.10.002.

Duval, M., Guilarte, V., Bartz, M., Alonso Escarza, M.J., Ben Arous, E., del Val, M., García Rodríguez, C., 2024. ESR dating of optically-bleached quartz grains: Evaluating measurement repeatability and reproducibility. Radiation Physics and Chemistry 215, 111313. doi: 10.1016/j.radphyschem.2023.111313.

Duval, M., Guilarte Moreno, V., 2012. Assessing the influence of the cavity temperature on the ESR signal of the Aluminum center in quartz grains extracted from sediment. Ancient TL 30, 11–16. doi: 10.26034/la.atl.2012.463.

Fattibene, P., Callens, F., 2010. EPR dosimetry with tooth enamel: A review. Applied Radiation and Isotopes 68, 2033–2116. doi: 10.1016/J.APRADISO.2010.05.016.

Guilarte, V., Duval, M., 2020. ESR dating of optically bleached quartz grains: Assessing the impact of different experimental setups on dose evaluations. Geochronometria 48, 179–190. doi: 10.2478/geochr-2020-0005.

Hoffmann, D., Mangini, A., 2002. Comparative studies on the CO_2-signal in tooth enamel and carbonates. Radiation Protection Dosimetry 101, 359–362. doi: 10.1093/OXFORDJOURNALS.RPD.A006001.

IAEA, 2002. Use of the Electron Paramagnetic Resonance Dosimetry with Tooth Enamel for Retrospective Dose Assessment. IAEA-TECDOC-1331. International Atomic Energy Agency, Austria , 57.

Liu, C.R., Yin, G.M., Gao, L., Bahain, J.J., Li, J.P., Lin, M., Chen, S.M., 2010. ESR dating of Pleistocene archaeological localities of the Nihewan Basin, North China – Preliminary results. Quaternary Geochronology 5, 385–390. doi: 10.1016/J.QUAGEO.2009.05.006.

Nilsson, J., Lund, E., Lund, A., 2001. The effects of UV-irradiation on the ESR-dosimetry of tooth enamel. Applied Radiation and Isotopes 54, 131–139. doi: 10.1016/S0969-8043(99)00275-4.

Niu, Y., Fan, Y., Qiao, Y., Lü, T., Li, C., Qi, L., Wang, S., Peng, S., Tan, Y., 2022. Chronostratigraphy of a loess-paleosol sequence in the western Chinese Loess Plateau based on ESR dating and magnetostratigraphy. Quaternary International 637, 1–11. doi: 10.1016/J.QUAINT.2022.08.005.

Prince, E., Tsukamoto, S., Grützner, C., Vrabec, M., Ustaszewski, K., 2024. Not too old to rock: ESR and OSL dating reveal Quaternary activity of the Periadriatic Fault in the Alps. Earth, Planets and Space 76, 1–27. doi: 10.1186/S40623-024-02015-6.

Sala-Ramos, R., Chacón, M.G., Aouraghe, H., Haddoumi, H., Morales, J.I., Rodríguez-Hidalgo, A., Tornero, C., Oujaa, A., Soto, M., Farkouch, M., Aissa, E.M., El Atmani, A., Duval, M., Arnold, L.J., Demuro, M., Blain, H.A., Piñero, P., Rivals, F., Burjachs, F., Tarriño, A., Álvarez-Posada, C., Souhir, M., Saladié, P., Pla-Pueyo, S., Larrasoña, J.C., Marín, J., Moreno, E., De Lombera-Hermida, A., Bartrolí, R., Lombao, D., García-Argudo, G., Ramírez, I., Díez-Canseco, C., Tomasso, S., Expósito, I., Allué, E., Noureddine, H., Mhamdi, H., Rhosne, H., Carrancho, A., Villalaín, J.J., Van der Made, J., Canals, A., Benito, A., Agustí, J., Parés, J.M., 2022. Evolución del asentamiento humano en la región de Aïn Beni Mathar – Guefaït (Jerada, Marruecos Oriental). Takurunna 10–11, 179–203.

Sholom, S., Chumak, V., 2008. Age-related peculiarities of tooth enamel as a natural EPR biodosimeter. Radiation Measurements 43, 823–826. doi: 10.1016/J.RADMEAS.2007.11.058.

Toyoda, S., Falguères, C., 2003. The method to represent the ESR signal intensity of the aluminium hole center in quartz for the purpose of dating. Advances in ESR Applications 20, 7–10.

Tsukamoto, S., Toyoda, S., Tani, A., Oppermann, F., 2015. Single aliquot regenerative dose method for ESR dating using X-ray irradiation and preheat. Radiation Measurements 81, 9–15. doi: 10.1016/J.RADMEAS.2015.01.018.

Voinchet, P., Pereira, A., Nomade, S., Falguères, C., Biddittu, I., Piperno, M., Moncel, M.H., Bahain, J.J., 2020. ESR dating applied to optically bleached quartz - A comparison with $^{40}Ar/^{39}Ar$ chronologies on Italian Middle Pleistocene sequences. Quaternary International 556, 113–123. doi: 10.1016/j.quaint.2020.03.012.

Yokoyama, Y., Falguères, C., Quaegebeur, J.P., 1985. ESR dating of quartz from Quaternary sediments: first attempts. Nuclear Tracks 10, 921–928. doi: 10.1016/0735-245X(85)90109-7.

Thesis Abstracts

Index

Tarfah Sayer Albaqami

Late Quaternary Palaeoenvironmental Reconstruction of Wadi Trubah in Western Saudi Arabia

May 2025
University of Sheffield, Sheffield, UK
Degree: Ph.D.
Supervisors: Mark D. Bateman, Robert G. Bryantz

While research into Quaternary environmental changes has taken place in the Central, Eastern, and southern regions of the Arabian Peninsula (AP) within Saudi Arabia, little paleoenvironment research has yet to be carried out in the western part of the AP, this is, even though the western part of Arabia is uniquely different from the eastern and central areas regarding climate and geology. Western Arabia is also critical in understanding past human migrations from Africa and the archaeological record of Arabia. To address the project's aims in reconstructing Late Quaternary environmental changes in wadi activity in the western region of Saudi Arabia and their relationship to regional environmental changes on the AP, a multiple methods approach using luminescence dating of the Wadi sedimentary archive, particle size analysis, and remote sensing was applied to map, understand, and model the fluvial drainage network. This research revealed the occurrence of major wet phases in the western part of the AP, which are MIS 9, 7, 3, and 1, which align with wet periods in other areas of the AP. Interestingly, no wet phase during MIS 5 has been found in the selected study area, indicating a need for further research.

Remote sensing has assisted in delineating the extensive stream network, which used to be active during intense precipitation during pluvial periods due to the combined climate-wind systems of the Indian Ocean Monsoon and the North African Summer Monsoon. Regarding palaeolakes, the research mapped 231 ancient lakes in the Harrat region, 93 interdune palaeolakes, and 4806 archaeological sites, which themselves suggest that Wadi Trubah had a favourable climate condition for human settlements.

Access to this thesis will be via https://etheses.whiterose.ac.uk/id/eprint/37731/

Renan Cassimiro Brito

Paleogeographic reconstruction of the middle Negro River during the Quaternary: a geomorphological-geochronological approach

July 2025
University of São Paulo, São Paulo, Brasil
Degree: Masters
Supervisors: Fabiano do Nascimento Pupim

The Negro River, the main tributary of the Solimões, drains the largest tropical watershed and sustains one of the most biodiverse ecosystems on the planet. Despite the well-documented influence of fluvial dynamics on Amazonian landscape evolution, the scarcity of absolute dating of sedimentary deposits limits the understanding of Quaternary paleohydrological changes. This gap hinders the chronological reconstruction of the geomorphological processes that have shaped the region's fluvial systems over the past 250,000 years. This research project aims to reconstruct the geological evolution of the middle Negro River during the Late Quaternary (<250 ka) through geomorphological mapping (terrace levels and floodplains), luminescence dating (11 quartz and 4 feldspar samples), and sediment provenance analysis (%BOSL1s). Terraces yielded ages between 297 ka and 103 ka (quartz) and between 390 ka and 302 ka (feldspar), while floodplains showed younger ages (31 ka to 2 ka). Quartz OSL sensitivity (%BOSL1s) increased from terraces (20–24 %) to floodplains (36–46 %), supporting Andean sediment sources with progressive reworking in floodplains. Three knickzones in the longitudinal profile correlate with lithological transitions (Içá Formation/Jauaperi Metamorphic Suite) and Pleistocene megafans that forced southwestward channel migration. Tributaries (Jaú and Unini rivers) exhibited distinct patterns: meandering reaches in less resistant rocks (Içá Formation) alternated with confined valleys in crystalline units (Jauaperi Suite). Terrace ages in the Cuiuni (103–328 ka) suggest that the disconnection between the Japurá paleochannels and the Negro River occurred more than 100 ka ago, recalibrating previous Holocene models. This hydrological reorganization likely influenced biogeographic patterns, including the Jaú-Negro endemism zone. Our results demonstrate that landscape evolution reflects the interplay of lithological controls, orbital-scale climate changes, and tectonic factors, providing a new

chronological framework for understanding Amazonian fluvial dynamics and their impacts on biodiversity.

This study was financially supported by the São Paulo Research Foundation (FAPESP, Grants 2023/10430-4 and 2024/07848-0) and the Coordination for the Improvement of Higher Education Personnel (CAPES, PROEX Grant 88887.805016/2023-00).

A PDF of this thesis can be downloaded from: https://doi.org/10.11606/D.44.2025.tde-09102025-072755

Garrett Richard Leo Marietta

A Bayesian model of beach ridge OSL chronology for determining Holocene lake-level changes of ancestral Lake Michigan

July 2025

Indiana University, Bloomington, United States of America

Degree: Masters

Supervisors: Jose Luis Antinao-Rojas, Brian Yanites, Henry Loope

Over the past three decades, beach ridges adjacent to the Great Lakes have provided researchers with key sedimentological and geochronological data used to construct Holocene paleohydrographs, records that reconstruct past lake levels and show trends in century-to-millennia scale hydrologic variability. Such paleohydrographs are critical for understanding changes in regional climate and lake-level trends. The beach ridges are a well-suited setting for optically stimulated luminescence (OSL) dating, as they contain eolian sand over foreshore deposits, both of which are fully bleached of all luminescence signal prior to deposition. Previous studies have shown that the beach ridges form during decadal periods of lake-level rise and fall and that the elevation of basal foreshore deposits is a close approximation to the elevation of the lake level at the high stand. These interpretations rely on the model of beach ridge formation where beach ridges must either form sequentially lakeward or be eroded.

This study focuses on the record of lake-level fluctuation preserved in a strandplain of beach ridges at the Wentworth Woods Nature Preserve (WWW) along the southwestern margin of Lake Michigan. OSL ages of the basal foreshore deposits should provide an estimate of age for the lake-level highstand. The basal foreshores from seven beach ridges were dated via OSL and ranged from 2.6 ± 0.3 ka to 6.2 ± 0.4 ka. Due to inconsistencies between the model for beach ridge formation and the ages determined through OSL that break this pattern, statistical analysis was pursued. Using Bayesian modeling of OSL ages across the strandplain, this study recalculated age ranges for the entire strandplain to be between 4.9 ± 0.2 ka and 5.2 ± 0.1 ka and reduced reporting error from a median of 7 % (356 yrs) to 2 % (113 yrs). Beyond chronologic resolution refinement, this analysis allows for century-scale interpretations of lake-level change and suggests that the age of the highest premodern lake-level, the peak of the Nipissing phase in the Great Lakes, is revised from its previously reported age of 4.5 ± 0.5 ka to be 5.1 ± 0.1 ka. This analysis not only improves the understanding of paleohydrology in the Great Lakes basin but also provides insight into lake-level change as a result of glacial isostatic and climate change.

A PDF of this thesis can be downloaded from: https://www.proquest.com/openview/62c9e771c70b7b887faede7f60bd3337/1?pq-origsite=gscholar&cbl=18750&diss=y

Hamdan Mahmal Saad Alghamdi

New dosimetry methods for radiological and nuclear emergency management

September 2025

Scottish Universities Environmental Research Centre, University of Glasgow, Glasgow, UK

Degree: Ph.D.

Supervisors: Prof. David Sanderson and Dr. Alan Cresswell

During all phases following a nuclear or radiological incident analyses of doses received by members of the public and responders are required. Rapid and reliable dose assessment is critical for the effective management of radiological emergencies; for medical triage, understanding exposure levels, directing protective actions, and conducting subsequent analyses of the impact of the incident. Current practice has been reviewed, highlighting the potential for near real-time luminescence dosimetry to assist with such assessments, including low dose response that supports public reassurance below doses of medical significance, using common materials present at the time of the incident. A number of materials which might be found in the immediate vicinity of people have previously been investigated with regard to their potential to act as radiation dosimeters. The work in this thesis investigates the properties of common household salt and talc, using portable Optically Stimulated Luminescence (OSL) and Infra-Red Stimulated Luminescence (IRSL) instruments capable of rapid measurements in the field. The potential of these materials to measure radiation levels and provide rapid, cost-effective insights into exposure patterns using new methods is explored. This approach aims to support emergency response strategies by leveraging accessible materials to improve decision-making in radiological incidents, bridging a key gap in large-scale radiation measurements and initial triage support.

Common salt has previously been shown to have the potential for retrospective dosimetry in the mGy dose range using laboratory instrumentation. This thesis investigates the use of portable instruments, with unprepared commercially sourced salt, in dose ranges below mGy. Responses from pulsed IRSL laboratory systems and portable OSL instruments were compared. For OSL measurements, detection limits of 7 µGy have been demonstrated, with detec-

tion limits of 30–340 µGy for the other instruments investigated. This work examines the effects of signal stability and sample storage conditions. The OSL signals initially show a brief decrease in luminescence during the first few days after irradiation, followed by a gradual increase with longer storage periods. Between days 8 and 64, the results remain relatively stable, which is crucial for dose estimation during both the early and later stages of responding to radiological emergencies, and methods for correcting for these signal variations at shorter and longer periods have been developed and demonstrated. However, exposure to light and moisture leads to a rapid loss of OSL signals. Three practical experiments were conducted using salt to simulate real accident scenarios, measure radiation, estimate dose, and compare the results with gamma systems (backpack). The first experiment was conducted under controlled laboratory conditions. The second mapped natural and artificial radiation fields in an outside environment. The final experiment mapped complex radiation fields within an accelerator laboratory. The results demonstrate that salt has considerable potential for use in dosimetry below mGy and that measurements can be conducted with portable OSL instruments. Furthermore, the results of the first two experiments compared well to theoretical doses and measurements with different systems. The results confirmed that this approach can provide reliable dose estimates for radiological accidents. The salt system has demonstrated its ability to map the spatial boundaries of radiation fields, serving as a low cost radiation mapping tool. Protocols must be instituted for testing and assessment during exercises, taking into account variables such as zeroing, ambient conditions, and the necessity for fading adjustments. The studies of talc focused on the optimal conditions for measuring the radiation-induced OSL signal using the SUERC Portable OSL Reader. It also addressed the inherent complexities associated with geological residual signals observed in talc sourced from Luzenac Pharma's packing line. This residual signal can be removed through thermal treatment, specifically at 400 °C for 1 h, after which the talc exhibits sufficient sensitivity to detect doses in the mGy range through to the radiologically significant range of 0.5 to 3 Gy, making it a promising candidate for field-deployable radiation assessment.

The fading data exhibit a complex decay pattern, suggesting the presence of multiple trap depths, with an initial signal loss of approximately 6 % within 24 h post-irradiation, escalating to a substantial 65 % reduction of the original OSL signal within 128 d at ambient temperature.

The work presented here has demonstrated that the novel approach of using salt or talc with portable OSL systems is capable of delivering dose estimates in the range from a few µGy to several Gy in near real-time, complementing existing techniques. To optimize this approach, comprehensive protocols should be developed for both testing exercises and evaluations, which could lead to wider acceptance of these approaches offering a robust, low-cost solution for rapid dose assessment for both emergency response and environmental dosimetry.

A PDF of this thesis can be downloaded from: https://theses.gla.ac.uk/85442/

Malika Singhal

High Radiation Dosimetry: Methodology Development

October 2025

Physical Research Laboratory, Ahmedabad, India

Degree: Ph.D.

Supervisors: Dr. Naveen Chauhan

Radiation dosimetry is the measurement of absorbed radiation dose (Gy = J kg^{-1}). Estimation of dose in natural minerals using luminescence emissions is an integral part of luminescence dating. The upper limit of luminescence dating is limited to ∼0.5 Ma. This limit is because of saturation of luminescence intensity with dose and depends on the capacity of the traps (defect sites) inside the crystal to accumulate charges produced during irradiation. The saturation is mineral-dependent and found to differ for different minerals. Quartz and feldspar are two ubiquitous minerals that are widely used in luminescence dating. The quest to increase the datable range of luminescence dating has been long, and many new traps (and their corresponding luminescence signals) in quartz and feldspar have been identified and probed to increase the datable range. However, the probed signals still face challenges in bridging the gap between laboratory calibrations and naturally acquired doses.

The present thesis attempts to develop a method to estimate high radiation doses (HRDs $\gtrsim$1 kGy) by exploring new minerals for high dose estimates and developing a better understanding of the luminescence mechanism in conventional minerals (quartz and feldspar) in the high dose regime. This thesis, for the first time, explores the luminescence characteristics of jarosite, a hydroxyl sulphate of metal and iron, because of its importance as a direct indicator of paleo-aridity (hence climate change) and its abundance and occurrence on Mars. Essential dosimetry properties like identification of traps, their thermal stability, bleaching, dose saturation, and athermal fading are studied. Thermoluminescence (TL) glow peaks appear around 100 °C, 150 °C, 300 °C, and 350 °C, with emissions recorded in the spectral range of 325–700 nm. Heating to 450 °C alters luminescence sensitivity without affecting the shape of glow curves, a finding supported by FTIR and CL-EDXS analyses. The 300 °C TL peak is thermally stable over geological time periods, with a lifetime of ∼0.3 million years (Ma) at 30 °C and ∼3 Ma at 10 °C ambient temperature, indicating suitability for dating older events in colder environments. Dose-response curves (DRCs) show saturation dose ranges from 590 to 1600 Gy for various traps probed by BSL, IRSL, pIRIR$_{225}$ and TL. Based on a terrestrial dose rate of ∼2 mGy a^{-1} and fading considerations, jarosite has the potential to date events up to ∼800 ka (constrained by the thermal stability to colder areas), while on Mars, where the dose rate is ∼65 mGy a^{-1}, the dating limit is approximately 25 ka.

The multi-spectral studies are conducted to understand the trapping, storage and recombination of charges in conventional minerals (quartz and feldspar) at HRDs. Experiments are conducted in the broad spectral window from 325–700 nm and are consequently narrowed down. Results show that quartz TL saturates in 10–18 kGy range, whereas feldspar TL saturates around 1–5 kGy, the range being sample-dependent. Since quartz provides a significant scope for estimating HRD, it is studied in detail in this thesis. The dose-response and saturation characteristics in quartz are found to be primarily controlled by the trapping centres rather than the recombination centres, with saturation doses showing minimal spectral dependence. Bleachability is found to be wavelength-dependent; longer-wavelength emissions exhibit reduced bleaching efficiency. Standard normalisation protocols, such as the zero or second glow normalisation, become unreliable beyond $\sim$1 kGy, leading to inconsistent sensitivity correction. Instead, normalisation approaches based on sample mass/weight should be used. These findings highlight the need for revised protocols at HRDs. The thesis further re-investigates the Blue Stimulated luminescence (BSL) from quartz at HRDs, which is known to saturate at $\sim$250 Gy, which is approximately 40 times less than the observed TL saturation. Results show that BSL measured on multiple aliquots of the same sample and compared by mass normalisation does not saturate as early as seen in Single Aliquot Regeneration (SAR) protocols. HRDs are better measured using Multiple Aliquot Additive Dose (MAAD) protocols in combination with alternative normalisation. Signals like zero-glow peak, annealed BSL, and annealed TL (blue emission) show reduced/negligible dependence on regeneration dose for the test signal, making them more suitable for constructing DRCs in the high-dose regime. Dose response curves generated using these normalisation methods show saturation around 5.8 kGy.

The thesis further uses the proposed methodology for two natural old geological settings: the Upper Shivaliks ($\sim$0.5–5 Ma) and the Charavathur formation ($>$2.5 Ma). In natural high-dose contexts, such as Shivalik sediments, where SAR-based curves show early saturation, the MAAD method proves particularly effective and could estimate higher radiation doses. In samples like those from Charavathur, where a low dose rate was estimated, the samples acquired an equilibrium between the trapping and detrapping due to thermal effects. MAAD accounts more appropriately for natural dose equilibrium, which cannot be explained by SAR. These findings highlight the limitations of SAR at high doses and suggests the use of MAAD protocols appropriately normalised for accurate dose estimation in old geological settings. However, the estimated doses are accompanied by large errors which need further investigation in the future.

A PDF of this thesis can be obtained by contacting the author: malikasinghal97@gmail.com.

Bibliography

Compiled by Jingran Zhang
From 01 June 2025 to 30 November 2025

Various geological applications

- aeolian

Bai, Y., Li, B., Rong, J., Chen, H., Zheng, J., Liu, J., Bao, T., Jin, J., Wang, C., 2025. Erosion rates of yardang landforms downstream of the Peacock River, NW China. Journal of Sedimentary Environments 10,1065-1077, http://doi.org/10.1007/s43217-025-00253-6

Dirnerová, D., Farkašovský, R., Hinca, R., 2025. Age of Blown Sand in the East Slovak Lowland—Case Study from Svätuše Sand Pit, Slovakia. Geosciences 15, 429, https://doi.org/10.3390/geosciences15110429

Hu, J., Hu, G., Yang, L., Guo, X., Zhang, J., Dong, Z., 2025. Periglacial aeolian activities in the Headwater Region of the Yellow River, northeastern Tibetan Plateau. Palaeogeography, Palaeoclimatology, Palaeoecology 671, 112984, http://doi.org/10.1016/j.palaeo.2025.112984

Kang, J., Zan, J., Yang, S., Li, P., Liu, L., Fang, X., Zhang, W., Azamdzhon, M., 2025. Luminescence dating of three loess-paleosol sequences in the western Pamir Plateau and their paleoclimatic implications during the Late Pleistocene. Palaeogeography, Palaeoclimatology, Palaeoecology 680, 113317, http://doi.org/10.1016/j.palaeo.2025.113317

Larsen, N.K., Siggaard-Andersen, M.L., Buylaert, J.P., Murray, A.S., Olsen, J., Ruter, A., Kjeldsen, K.K., Bjork, A.A., Mikkelsen, N., Kjær, K.H., 2025. Increased aeolian activity linked to Neoglacial cooling and glacier advance in southern Greenland. Boreas 54, 382-394, http://doi.org/10.1111/bor.12688

Shi, Y., E, C., Xu, C., Yan, W., Sun, Y., Zhang, Z., Zhang, J., Peng, Q., 2025. Reconstructing aeolian activities and borders shifts of the Gonghe Sandy Lands since the last Glacial Maximum. Geomorphology 478, 109706, http://doi.org/10.1016/j.geomorph.2025.109706

Song, H., Liang, Z., Duan, M., Liu, M., Liu, L., Chen, Z., Han, S., Zhang, H., Zhou, C., 2025. Quaternary stratigraphy of Bayan borehole in eastern Songnen Plain and its paleoclimate significance. Scientific Reports 15, 32027, http://doi.org/10.1038/s41598-025-15418-6

Zhang, Z., E, C., Sun, Y., Zhang, J., Shi, Y., Peng, Q., Xianba, J., 2025. Holocene paleoclimate variations and East Asian monsoonal dynamics revealed by high-resolution OSL dating of aeolian sediments in the Qinghai Lake Basin. Earth Surface Processes and Landforms 50, e70112, http://doi.org/10.1002/esp.70112

Zhong, J., Lai, P., Liao, W., Lai, Z., Bae, C.J., Wang, W., Vandenberghe, J., 2025. The Late Quaternary Aeolian Deposits in the Subtropical Bose–Bubing Basins, Southern China. Quaternary 8, 70, http://doi.org/10.3390/quat8040070

- coastal

Gernant, C., Simms, A.R., DeWitt, R., Theilen, B., Garcia, C.N., Goebel, M., 2025. Insights into the sea-level history of the South Shetland Islands from ground penetrating radar on Livingston Island, Antarctica. Quaternary Science Reviews 359, 109363, http://doi.org/10.1016/j.quascirev.2025.109363

Gkouma, M., Karkanas, P., Koukousioura, O., Syrides, G., Chalkioti, A., Tsakalos, E., Ntinou, M., Efstratiou, N., 2025. Exploring Continental and Submerged Paleolandscapes at the Pre-Neolithic Site of Ouriakos, Lemnos Island, Northeastern Aegean, Greece. Quaternary 8, 42, http://doi.org/10.3390/quat8030042

Gouveia, M.P., Cunha, P.P., Martins, A.A., Stokes, M., Gomes, A., Falguères, C., Voinchet, P., Bahain, J.-J., Pereira, T., Figueiredo, S., Shao, Q., Tombret, O., 2025. Plio-Quaternary coastal uplift along the western Iberian Margin: insights from dated marine terraces (Peniche, Portugal). Quaternary International 747, 109954, http://doi.org/10.1016/j.quaint.2025.109954

Hou, C., Jin, J., Ma, M., Liu, G., Ling, Z., Wei, J., Xu, D., 2025. Temporal variation of luminescence sensitivity and environmental changes during the mid-late Holocene recorded in estuarine coastal deposits from South China. Catena 255, 109022, http://doi.org/10.1016/j.catena.2025.109022

Kim, D.-E., Kwon, C.W., Lee, T.-H., Lee, H.J., Lee, H., 2025. Timing of Late Pleistocene marine terrace exposure using OSL and ^{10}Be dating: Constraints on the tectonic uplift of the southeastern Korean Peninsula. Progress in Physical Geography: Earth and Environment 49, 377-399, http://doi.org/10.1177/03091333251344158

Leknettip, S., Chawchai, S., Bissen, R., Dubois, N., Fülling, A., Preusser, F., 2025. Holocene sea-level changes and the influence of storms on beach ridge formation in the Lower Gulf of Thailand. Sedimentology 72, 1402-1429, http://doi.org/10.1111/sed.70007

Leknettip, S., Chawchai, S., Fülling, A., Preusser, F., 2025. Pleistocene sea-level and environmental changes during glacial-interglacial cycles recorded in beach ridges of the Thai-Malay Peninsula. Quaternary Science Reviews 364, 109464, http://doi.org/10.1016/j.quascirev.2025.109464

Maruyama, M., Hori, K., Tamura, T., Ishii, Y., Seike, K., Nakanishi, T., Hong, W., 2025. Beach ridge formation and Holocene relative sea-level changes in the southern Sendai coastal plain, northern Japan. Geomorphology 488, 109957, http://doi.org/10.1016/j.geomorph.2025.109957

Moreira, V.B., Lämmle, L., D'Aniello, M., Da Conceição, F.T., Donadio, C., Perez Filho, A., 2025. The role of Holocene climate dynamics in the modeling of fluviomarine terraces in the northeastern Brazilian coast. Quaternary International 747, 109965, http://doi.org/10.1016/j.quaint.2025.109965

Perazzotti, F., Valle, L.d., Cossu, G., Pascucci, V., Fornós, J.J., 2025. Paleoenvironmental changes and sea-level fluctuations record at Punta de s'Avançada, Mallorca Island. Quaternary International 735, 109839, http://doi.org/10.1016/j.quaint.2025.109839

Schomacker, A., Alexanderson, H., Farnsworth, W.R., Furze, M.F.A., Kjellman, S.E., Kirchner, N., Erstorp, E.S., Noormets, R., Jomelli, V., Ingólfsson, Ó., 2025 Weichselian–Holocene glacial history of the Sjuøyane archipelago, northern Svalbard. Boreas 54, 288-304, http://doi.org/10.1111/bor.12673

Simms, A.R., DeWitt, R., Bradley, S.L., Huffman, E., Best, L., Bradwell, T., Lloyd, J.M., Kachuck, S.B., 2025. Was Scotland covered by an ice sheet during Marine Isotope Stage 4? Insights from the pre-Last Glacial Maximum marine terraces of northwest Scotland. Journal of Quaternary Science 40, 1097-1105, http://doi.org/10.1002/jqs.70000

Tanigawa, K., Tamura, T., Komori, K., Negoro, Y., 2025. Holocene coastal barrier dune development and its influence on marine inundations: An example from the Kochi coast facing the Nankai Trough, southern Japan. Geomorphology 486, 109887, http://doi.org/10.1016/j.geomorph.2025.109887

Wang, Y., Meltzner, A.J., Quye-Sawyer, J., Yang, H., Pu, Y., Qin, J., Aung, L.T., Aw, Z., Pamintuan, A.D.A., Ramos, N.T., 2025. Uplift, tilting, and underlying structures of coastal northwestern Luzon, Philippines, deduced from marine terraces. Quaternary Science Reviews 358, 109347, http://doi.org/10.1016/j.quascirev.2025.109347

Xu, Z., Han, Y., Yan, B., Li, M., Jiang, R., Tian, R., Liu, B., Zhu, Z., Yuan, W., Lai, Z., 2025. Luminescence dating of core sediments from the southern coastal Bohai Sea, China, and its implications for transgression history during the Late Quaternary. Frontiers in Marine Science 12, 1606184, http://doi.org/10.3389/fmars.2025.1606184

Yüksel, M., Deniz, F., Ünsal, E., 2025. ANN-Based Prediction of OSL Decay Curves in Quartz from Turkish Mediterranean Beach Sand. Crystals 15, 733, http://doi.org/10.3390/cryst15080733

- earthquakes and tectonic activity

Gaidzik, K., Ramírez-Herrera, M.-T., Dominguez, L.A., Coca, O., Forman, S.L., Vargas-Espinosa, V., Arenas, L.F., 2025. Geomorphic and paleoseismic evidence for active faulting along La Venta Fault, Guerrero, Mexican subduction Forearc. Geomorphology 485, http://doi.org/10.1016/j.geomorph.2025.109869

Goswami, C.C., Štěpančíková, P., Singh, A., Jaiswal, M.K., Jana, P., 2025. "Fault dynamics and paleoseismic evidence in the Darjeeling-Sikkim Himalayan foothills: A study of fault-controlled landscapes". Geomorphology 482, 109869, http://doi.org/10.1016/j.geomorph.2025.109802

Gutiérrez, F., Haghighi, M.H., Ilyati, I., Motagh, M., del Val, M., 2025. Diapiric and tectonic geomorphology of the river-damming Jahani salt extrusion associated with the strike-slip Kareh Bas Fault, including DInSAR displacement data (Zagros Mountains, Iran). Geomorphology 488, 109955, http://doi.org/10.1016/j.geomorph.2025.109955

Hu, X., Ju, N., Zhao, J., Feng, Q., Zhao, W., Huang, J., Xie, M., 2025. Reservoir impoundment induced the revival of toppling paleo-landslide in the upper reaches of the Yellow River: a case of Darou landslide. Landslides 22, 3743-3757, http://doi.org/10.1007/s10346-025-02570-3

Karlstrom, K.E., Baisan, C.H., Kring, D.A., Hereford, R., Turney, C., Hogg, A., Norman, L.M., O'Brien, P., Palmer, J.G., Rittenour, T.M., Ballensky, J., Crossey, L.J., 2025. Grand Canyon landslide-dam and paleolake triggered by the Meteor Crater impact at 56 ka. Geology 53, 821-826, http://doi.org/10.1130/g53571.1

Langridge, R.M., Howarth, J.D., Coffey, G.L., Villamor, P., Ries, W.F., Cochran, U.A., Sagar, M., La Greca, J., Rhodes, E.J., Saha, S., Dahl, J., 2025. A multi-event paleoseismic record from the northern Alpine Fault at Marble Hill, Aotearoa New Zealand. Geomorphology 489, 109945, http://doi.org/10.1016/j.geomorph.2025.109945

LaPlante, A.A., Regalla, C.A., Sethanant, I., Mahan, S.A., Gray, H.J., 2025. Spatiotemporal Variations in Strain Release and Seismic Rupture in Multifault Systems: An Example from Panamint Valley, Southeastern California. Lithosphere 2024, http://doi.org/10.2113/2024/lithosphere_2024_187

Mondal, S., Das, S., Chauhan, N., Dey, S., 2025. Millennial-Scale Slip Rates Along Blind Himalayan Frontal Thrust: Findings From Chalsa-Gorubathan Recess in East-Central Himalaya. Terra Nova 37, 395-402, http://doi.org/10.1111/ter.70000

Prince, E., Tsukamoto, S., Grützner, C., Bülhoff, M., Ustaszewski, K., 2025. Deciphering Pleistocene Fault Activity in the Eastern Alps: Dating Fault Gouges With Electron Spin Resonance and Optically Stimulated Luminescence. Tectonics 44, e2024TC008662, http://doi.org/10.1029/2024tc008662

Srivastava, E., Gadhavi, M., Sharma, N., Kumar, P., Malik, J.N., Sulli, A., 2025. Geomorphic imprints of long- and short-term deformation in the Kachchh Intraplate Region (Western India). Geomorphology 486, 109890, http://doi.org/10.1016/j.geomorph.2025.109890

Tyagi, A.K., Kumar, D., Murari, M.K., Singh, R.N., Singhvi, A.K., 2025. Viscous heating in sediments as a 'Zeroing' mechanism in luminescence dating of sand dikes for paleoseismological investigations. Earth and Planetary Science Letters 670, 119578, http://doi.org/10.1016/j.epsl.2025.119578

Wang, K., Li, X., Shi, W., Feng, X., Yang, Q., Li, J., Xu, Z., Peng, Z., Xu, S., Xiong, Y., Lin, M., 2025. A Typical Riedel Shear Pattern of Active Faults in the Laolongwan Basin, Northeastern Tibetan Plateau. Journal of Earth Science 36, 1906-1922, http://doi.org/10.1007/s12583-023-1831-5

Xin, C., Yan, S., Li, H., Dai, X., Liu, T., Wang, J., 2025. Cenozoic Multiphasic Activity and Mesozoic Basin-Control Role of the Dingri–Gangba Fault, Southern Tibet: An Integrated Study of Structural Analysis, Stratigraphic Correlation, and ESR Geochronology. Geosciences 15, 440, http://doi.org/10.3390/geosciences15110440

Yao, Y., Shao, Y., Zhang, B., 2025. Preliminary Study on the Activity of the Rupture Zone in the Eastern Segment of the Ba Co Fault in Ngari Prefecture, Tibet. Geosciences 15, 377, http://doi.org/10.3390/geosciences15100377

Zhang, X., Zhong, N., Yu, H., Yu, X., Li, H., 2025. Geometric Structural Characteristics and Tectonic Significance of the Litang Fault Zone, Southeastern Margin of the Tibetan Plateau. Acta Geologica Sinica - English Edition 99, 942-960, http://doi.org/10.1111/1755-6724.15330

- fluvial

Arzhannikova, A.V., Arzhannikov, S.G., Tetenkin, A.V., Chebotarev, A.A., Timofeeva, I.V., Efremova, U.S., Gladkochub, E.A., Bryanskiy, N.V., 2025. Chronology of glacial megafloods in the Baikal-Patom Upland (South Siberia): New geochronological constraints. Quaternary International 749, 110004, http://doi.org/10.1016/j.quaint.2025.110004

Cao, P., Zhang, Y., Zhu, Y., Wang, N., Huang, C.C., Shi, X., Pang, J., Li, Y., Zhou, J., Wang, S., Jin, Y., Li, M., Huang, X., Shen, M., Dong, J., 2025. Evolutionary history of a paleo-oxbow lake in the Yellow River within the Zoige Basin, NE Tibetan Plateau. Quaternary International 745, 109938, http://doi.org/10.1016/j.quaint.2025.109938

Carling, P.A., Meshkova, L., Srivastava, A., Kinnaird, T., Ding, Z., Robinson, R., Darby, S.E., Fan, X., 2025. Fluvial terraces of the lower Mekong River reflect quaternary global sea level fluctuations as a likely response to Himalayan glacial/deglacial runoff. Geomorphology 480, 109756, http://doi.org/10.1016/j.geomorph.2025.109756

Collins, B.D., Schmidt, A.H., Harrell, S., Aalto, R., Feathers, J., Tang, Y., 2025. Holocene and recent valley-bottom sediment storage decouples natural and anthropogenic hillslope erosion from sediment delivery to streams at time scales of 101–104 yr in a third-order Yangtze River basin, Sichuan, China. Quaternary Research 128, 9-31, http://doi.org/10.1017/qua.2025.22

Dixon, T., Rudd, R., Kemp, J., Marx, S., Moss, P., Callow, J.N., Hall, P.A., Hua, Q., McGowan, H., 2025. Hydroclimate variability in the eastern Kimberley, Australia, since the last deglaciation. Journal of Quaternary Science 40, 893-912, http://doi.org/10.1002/jqs.3710

Duan, M., Neubauer, F., Robl, J., Zhou, X., Argentin, A.-L., Liebl, M., Dong, Y., Shi, X., Zhang, S., Peng, H., 2025. The northward expansion of the Tibetan Plateau: Topographic evidence from the Bogda Mts. – southern Junggar Basin coupling system, northwest China. Quaternary Science Reviews 362, 109402, http://doi.org/10.1016/j.quascirev.2025.109402

Feng, S., Tan, C., Plink-Björklund, P., Shan, X., Li, S., Li, S., Yu, X., Chen, L., Ji, H., 2025. Sedimentary response to glacial-interglacial cycles in an alluvial fan at the marginal East Asian monsoon zone, northern China. Sedimentology 72, 1375-1401, http://doi.org/10.1111/sed.70006

Geis, A.-L., Sontag-González, M., Kolb, T., Jain, M., Fuchs, M., 2025. Multi-method luminescence dating of late Cenozoic northern Upper Rhine Graben fluvial sediments. Quaternary Geochronology 90, 101689, http://doi.org/10.1016/j.quageo.2025.101689

Hou, C., Jin, J., Ma, M., Liu, G., Ling, Z., Wei, J., Xu, D., 2025. Temporal variation of luminescence sensitivity and environmental changes during the mid-late Holocene recorded in estuarine coastal deposits from South China. Catena 255, 109022, http://doi.org/10.1016/j.catena.2025.109022

Huang, X., Wang, P., Fang, Y., Ye, H., Liu, F., 2025. Hydrodynamics of late Quaternary outburst floods along the Yigong River, Eastern Himalayan Syntaxis. Palaeogeography, Palaeoclimatology, Palaeoecology 676, 113168, http://doi.org/10.1016/j.palaeo.2025.113168

Ishii, Y., 2025. Alluvial fan aggradation during the MIS 6 sea-level lowstand in the lower reach of the Tenryu River, Japan. Earth Surface Processes and Landforms 50, e70146, http://doi.org/10.1002/esp.70146

Lai, Z., Liu, Y., Wu, Z., Xu, Y., Fang, Z., Montgomery, D.R., 2025. Headward incision of large rivers in response to glacial sea level fall. Science Advances 11, eadr5446, http://doi.org/10.1126/sciadv.adr5446

Langridge, R.M., Howarth, J.D., Coffey, G.L., Villamor, P., Ries, W.F., Cochran, U.A., Sagar, M., La Greca, J., Rhodes, E.J., Saha, S., Dahl, J., 2025. A multi-event paleoseismic record from the northern Alpine Fault at Marble Hill, Aotearoa New Zealand. Geomorphology 489, 109945, http://doi.org/10.1016/j.geomorph.2025.109945

Li, X., Chen, D., Pan, B., Garzanti, E., Huang, D., Wang, K., Chen, D., Hu, D., Liu, W., Fu, X., 2025. Drainage evolution in response to the growing northeastern Tibetan Plateau: Provenance analysis from drill core of the Jinta Basin (NW China). Geomorphology 486, 109892, http://doi.org/10.1016/j.geomorph.2025.109892

Li, Y., Lu, P., Chen, P., Wang, H., Yang, S., Zhao, X., Liao, Y., Tian, Y., Wang, Z., Mo, D., 2025. Landform basis for the rise of early cities in the upper Jialu river basin, central China. Quaternary International 735, 109842, http://doi.org/10.1016/j.quaint.2025.109842

Liu, X., Quan, C., Liu, Z., Li, R., 2025. Late Pleistocene megalake system in the Yinchuan-Hetao rifting basins, upper reaches of the Yellow River. Quaternary Science Reviews 365, 109473, http://doi.org/10.1016/j.quascirev.2025.109473

Liu, Z., Yang, J., Zhao, H., Song, L., Wang, C., 2025. Luminescence Dating of Holocene Fluvial Sediments from the Daluze Area in the North China Plain. Water 17, 1942, http://doi.org/10.3390/w17131942

Mahadev, Behera, D., Kumar, P., Jaiswal, M.K., Singh, A.K., 2025. A Terrestrial record of ~3000 years of extreme floods from the Kaveri and adjacent river basins, Tamil Nadu, India. Quaternary International 738, 109856, http://doi.org/10.1016/j.quaint.2025.109856

Marik, M., Serra, E., Rixhon, G., Preusser, F., 2025. Luminescence dating of alluvial sediments from the Quaternary fan–terrace sequence of the lower Bruche valley, Upper Rhine Graben, France. E&G Quaternary Science Journal 74, 169-192, http://doi.org/10.5194/egqsj-74-169-2025

Martín-Perea, D.M., Medialdea, A., Marín, J., Abellán, N., Solano-Megías, I., Arteaga, C., Rodríguez-Hidalgo, A., Uribelarrea, D., Arroyo, X., Gidna, A., Mabulla, A., Maíllo-Fernández, J.M., 2025. Geology and chronology of the Ndutu and Naisiusiu type sites: implications for Middle and Later Stone Age occupations at Olduvai Gorge (Tanzania). Quaternary Science Reviews 368, 109578, http://doi.org/10.1016/j.quascirev.2025.109578

Moreira, V.B., Lämmle, L., D'Aniello, M., Da Conceição, F.T., Donadio, C., Perez Filho, A., 2025. The role of Holocene climate dynamics in the modeling of fluviomarine terraces in the northeastern Brazilian coast. Quaternary International 747, 109965, http://doi.org/10.1016/j.quaint.2025.109965

Panin, A., Zaretskaya, N., Baranov, D., Utkina, A., Kurbanov, R., 2025. Late Quaternary architecture of the lower Vychegda valley, northern European Russia: Insights into landscape dynamics at the eastern margin of the last Scandinavian ice sheet. Earth Surface Processes and Landforms 50, e70202, http://doi.org/10.1002/esp.70202

Seidel, P., Rolf, M., Holzinger, A., Gröbner, M., Riedesel, S., Laermanns, H., Feldhaar, H., Laforsch, C., Loeder, M.G.J., Bogner, C., 2025. Vertical distribution and post-depositional translocation of microplastics in a Rhine floodplain soil. Microplastics and Nanoplastics 5, 34, http://doi.org/10.1186/s43591-025-00142-9

Shang, L., Zha, X., Huang, C., Zhou, Y., Pang, J., Li, Y., Wang, Z., 2025. Reconstructing the magnitudes of Holocene extraordinary floods in the upper Huai River, China. Quaternary Science Reviews 359, 109371, http://doi.org/10.1016/j.quascirev.2025.109371

Shi, T., Miao, X., Shen, H., Zhai, Q., Wang, S., 2025. Extreme flood events in the Yi and Shu river basins of the Haidai region (Shandong Province, China) during the late Holocene: Implications for future risk prediction. Palaeogeography, Palaeoclimatology, Palaeoecology 674, 113011, http://doi.org/10.1016/j.palaeo.2025.113011

Stanistreet, I.G., Stollhofen, H., Smedley, R.K., Fenn, K., Ambrose, S.H., Njau, J.K., Schick, K., Toth, N., 2025. Luminescence and radiocarbon dating the Naisiusiu Beds type section and timing of the Middle Stone Age/Later Stone Age transition at Olduvai Gorge, Tanzania. Journal of Human Evolution 207, 103675, http://doi.org/10.1016/j.jhevol.2025.103675

Su, Q., Wang, X., Yuan, D., Jiang, J., Lai, Z., Zhang, L., Sun, H., Li, H., Huang, X., Zhou, K., Li, H., 2025. Temporally staggered formation of the Middle Pleistocene terrace in the Gonghe Basin (northeastern Tibetan Plateau) and the evolution of the Upper Yellow River. Geological Society of America Bulletin 138, 744-756, http://doi.org/10.1130/b38225.1

Tian, R., Yan, B., He, C., Yuan, W., Lin, P., Song, Y., Liu, B., Liu, Y., Miao, X., Lai, Z., 2025. Paleolakes in the lower Yellow River plain since the last deglaciation: age, distribution, and mechanism. Catena 259, 109315, http://doi.org/10.1016/j.catena.2025.109315

Westell, C., Roberts, A., Morley, M.W., Moffat, I., Hernandez, V.C., Spooner, N.A., McDonnell, K., Rudd, R., Petchey, F., 2025. Life beyond the lakes: An analysis and implications of a Pleistocene combustion feature on the Pike River in South Australia. Journal of Archaeological Science 180, 106264, http://doi.org/10.1016/j.jas.2025.106264

Yang, A., Hu, K., Wang, H., Liu, W., Zhang, Q., Liu, S., Li, H., 2025. Evolution of a landslide-dammed lake during the Holocene: Records from lacustrine and fan-delta successions in southeastern Tibet. Earth Surface Processes and Landforms 50, e70104, http://doi.org/10.1002/esp.70104

Yuan, W., Liu, B., Wu, Z., Wang, Y., Sun, Z., Zhou, X., Tian, R., Yan, B., Lai, Z., 2025. Luminescence dating of core sediments from Jining of Shandong Province in the lower Yellow River Plain and its geomorphological implications. Palaeogeography, Palaeoclimatology, Palaeoecology 675, 113042, http://doi.org/10.1016/j.palaeo.2025.113042

Yuan, W., Pan, B., Yi, C., Wei, M., Yan, P., Zhao, J., Liu, X., Xu, X., Dong, G., Li, X., 2025. Holocene geomorphic process recorded by OSL dating of Linggo Co delta and outwash terraces from the Puruogangri area in the central Tibetan Plateau. Earth Surface Processes and Landforms 50, e70169, http://doi.org/10.1002/esp.70169

Yuskar, Y., Kranz-Bartz, M., Schmidt, C., Choanji, T., Lane, S., King, G., 2025. A first chronological framework for fluvial terrace deposits of the Kampar Kanan River, Indonesia. Geochronometria 52, 205688, http://doi.org/10.20858/geochr/205688

Zhao, Y., Fan, N., An, Y., Nie, J., Abell, J.T., Jin, Z., Wang, C., Nie, R., Liu, X., 2025. Co-evolution of palaeolakes in the Hetao Basin and the Yellow River over the last 500 ka. Palaeogeography, Palaeoclimatology, Palaeoecology 674, 113038, http://doi.org/10.1016/j.palaeo.2025.113038

- cave sediments

Padoan, L., Karmann, I., Granger, D., Laureano, F.V., Paes de Almeida, R., Cruz, F.W., Sawakuchi, A.O., Fonseca, E.S., Meza, A.B., Gallas, J.D.F., 2025. Cave sediment chronology and erosion rates in the São Desidério karst reveal a million-year-scale landscape evolution of the Central Brazilian Plateau. Geomorphology 483, 109820, http://doi.org/10.1016/j.geomorph.2025.109820

Hudson, M., Paces, J., Darryl, G., Rodrigues, K., Keen-Zebert, A., Bitting, C., Turner, K., Sapkota, K., 2025. Two million years of climate-driven cave-sediment aggradation and valley incision in the southern Ozark Plateau from Fitton Cave, northern Arkansas, USA. Quaternary Research 128, 102-125, http://doi.org/10.1017/qua.2025.14

- glacial and periglacial

Arzhannikova, A.V., Arzhannikov, S.G., Tetenkin, A.V., Chebotarev, A.A., Timofeeva, I.V., Efremova, U.S., Gladkochub, E.A., Bryanskiy, N.V., 2025. Chronology of glacial megafloods in the Baikal-Patom Upland (South Siberia): New geochronological constraints. Quaternary International 749, 110004, http://doi.org/10.1016/j.quaint.2025.110004

Gernant, C., Simms, A.R., DeWitt, R., Theilen, B., Garcia, C.N., Goebel, M., 2025. Insights into the sea-level history of the South Shetland Islands from ground penetrating radar on Livingston Island, Antarctica. Quaternary Science Reviews 359, 109363, http://doi.org/10.1016/j.quascirev.2025.109363

Li, H., Yao, P., Ou, X., Xu, Y., Yang, K., Liu, J., 2025. Luminescence dating of glaciofluvial deposits using single-grain K-feldspar in the Urumqi River headwaters of the Tianshan Mountains. Progress in Geography 44, 2203-2214, http://doi.org/10.18306/dlkxjz.2025.10.015

Schomacker, A., Alexanderson, H., Farnsworth, W.R., Furze, M.F.A., Kjellman, S.E., Kirchner, N., Erstorp, E.S., Noormets, R., Jomelli, V., Ingólfsson, Ó., 2025 Weichselian–Holocene glacial history of the Sjuøyane archipelago, northern Svalbard. Boreas 54, 288-304, http://doi.org/10.1111/bor.12673

Sharma, U., Ray, Y., Sagwal, S., Sangode, S.J., 2025. Spatio-temporal variability of Quaternary glaciation in the arid alpine Spiti basin, Trans-Himalaya: Insights from luminescence dating and sedimentological analyses. Palaeogeography, Palaeoclimatology, Palaeoecology 679, 113322, http://doi.org/10.1016/j.palaeo.2025.113322

Simms, A.R., DeWitt, R., Bradley, S.L., Huffman, E., Best, L., Bradwell, T., Lloyd, J.M., Kachuck, S.B., 2025. Was Scotland covered by an ice sheet during Marine Isotope Stage 4? Insights from the pre-Last Glacial

Maximum marine terraces of northwest Scotland. Journal of Quaternary Science 40, 1097-1105, http://doi.org/10.1002/jqs.70000

- lacustrine

Fitzsimmons, K.E., Fischer, M.L., Smith, T., Lauer, T., Nowatzki, M., Mishra, K., Murray-Wallace, C.V., 2025. Long-term hydrologic connectivity on the Australian dryland margins: Evidence from the Willandra Lakes World Heritage Area over the last 60 ky. Journal of Quaternary Science 40, 876-892, http://doi.org/10.1002/jqs.3717

Gutiérrez, F., Haghighi, M.H., Ilyati, I., Motagh, M., del Val, M., 2025. Diapiric and tectonic geomorphology of the river-damming Jahani salt extrusion associated with the strike-slip Kareh Bas Fault, including DInSAR displacement data (Zagros Mountains, Iran). Geomorphology 488, 109955, http://doi.org/10.1016/j.geomorph.2025.109955

Karlstrom, K.E., Baisan, C.H., Kring, D.A., Hereford, R., Turney, C., Hogg, A., Norman, L.M., O'Brien, P., Palmer, J.G., Rittenour, T.M., Ballensky, J., Crossey, L.J., 2025. Grand Canyon landslide-dam and paleolake triggered by the Meteor Crater impact at 56 ka. Geology 53, 821-826, http://doi.org/10.1130/g53571.1

Larsen, N.K., Siggaard-Andersen, M.L., Buylaert, J.P., Murray, A.S., Olsen, J., Ruter, A., Kjeldsen, K.K., Bjork, A.A., Mikkelsen, N., Kjær, K.H., 2025. Increased aeolian activity linked to Neoglacial cooling and glacier advance in southern Greenland. Boreas 54, 382-394, http://doi.org/10.1111/bor.12688

Liu, X., Quan, C., Liu, Z., Li, R., 2025. Late Pleistocene megalake system in the Yinchuan-Hetao rifting basins, upper reaches of the Yellow River. Quaternary Science Reviews 365, 109473, http://doi.org/10.1016/j.quascirev.2025.109473

Long, H., Zhang, J., Zhang, S., Hou, Y., Wu, Y., Yang, N., Zhang, C., Cheng, L., Zhao, Z., Cheng, J., Shen, J., 2025. The westerlies-monsoon interaction shaped asymmetric lake expansions over the Tibetan Plateau in warming periods. Science Bulletin 70, 3245-3254, http://doi.org/10.1016/j.scib.2025.07.023

Michalec, G., Sikora, R., Winiarska-Kabacińska, M., Odsuren, D., Wójcik, A., Moska, P., Szmit, M., Bazargur, D., Bobrowski, P., Jórdeczka, M., Szykulski, J., Muntowski, P., Gałaś, A., Gunchinsuren, B., Masojć, M., 2025. Geoarchaeological research on site formation process, paleoenvironment, and human behaviors in the early Holocene of the Gobi Desert, Mongolia. PLOS One 20, e0330209, http://doi.org/10.1371/journal.pone.0330209

Tian, R., Yan, B., He, C., Yuan, W., Lin, P., Song, Y., Liu, B., Liu, Y., Miao, X., Lai, Z., 2025. Paleolakes in the lower Yellow River plain since the last deglaciation: age, distribution, and mechanism. Catena 259, 109315, http://doi.org/10.1016/j.catena.2025.109315

Yang, A., Hu, K., Wang, H., Liu, W., Zhang, Q., Liu, S., Li, H., 2025. Evolution of a landslide-dammed lake during the Holocene: Records from lacustrine and fan-delta successions in southeastern Tibet. Earth Surface Processes and Landforms 50, e70104, http://doi.org/10.1002/esp.70104

Zhao, H., Liu, W., Li, X., Yang, A., Zhou, L., Zhou, Y., Yang, S., 2025. The genesis, evolution, and geomorphological significance of the Kangkong Paleolake in the PhungQu Basin of southern Tibet. Geomorphology 488, 109964, http://doi.org/10.1016/j.geomorph.2025.109964

Zhao, H., Zhang, S., Sheng, Y., Yang, Z., Wang, K., Chen, F., 2025. Timing of mega-lakes in the central-southern Tibetan Plateau constrained by K-feldspar single-grain pIRIR dating of paleo-shorelines. Global and Planetary Change 254, 104989, http://doi.org/10.1016/j.gloplacha.2025.104989

Zhao, Y., Fan, N., An, Y., Nie, J., Abell, J.T., Jin, Z., Wang, C., Nie, R., Liu, X., 2025. Co-evolution of palaeolakes in the Hetao Basin and the Yellow River over the last 500 ka. Palaeogeography, Palaeoclimatology, Palaeoecology 674, 113038, http://doi.org/10.1016/j.palaeo.2025.113038

- landslide

Bispo, C.O., Listo, F.L.R., Listo, D.G.S., 2025. Shallow translational landslides on the east face of Araripe Plateau, northeastern Brazil: SHALSTAB model and Optically Stimulated Luminescence (OSL) dating. Journal of South American Earth Sciences 162, 105582, http://doi.org/10.1016/j.jsames.2025.105582

Yang, A., Hu, K., Wang, H., Liu, W., Zhang, Q., Liu, S., Li, H., 2025. Evolution of a landslide-dammed lake during the Holocene: Records from lacustrine and fan-delta successions in southeastern Tibet. Earth Surface Processes and Landforms 50, e70104, http://doi.org/10.1002/esp.70104

- loess

Ali, A., Achyuthan, H., Sangode, S.J., Jaiswal, M., Shah, R.A., 2025. Palaeoclimate Dynamics in Kashmir Valley: Loess Palaeosols and shifts in Mineral Magnetism during MIS 3. Journal of the Geological Society of India 101, 968-973, http://doi.org/10.17491/jgsi/2025/174193

Chang, Q., Miao, X., Xie, X., Lai, Z., 2025. Luminescence dating and the sedimentary pattern of loess on the Tibetan Plateau. Aeolian Research 74, 100994, http://doi.org/10.1016/j.aeolia.2025.100994

Hu, X., Zhang, Y., Li, C.a., Li, G., Liu, J., Li, Y., Su, J., Jia, M., 2025. Provenance of Wushan Loess in the Yangtze Three Gorges Region: Insights from Detrital Zircon U-Pb Geochronology and Late Pleistocene East Asian Monsoon Variations. Minerals 15, 1180, http://doi.org/10.3390/min15111180

Kang, J., Zan, J., Yang, S., Li, P., Liu, L., Fang, X., Zhang, W., Azamdzhon, M., 2025. Luminescence dating of three loess-paleosol sequences in the western Pamir Plateau and their paleoclimatic implications during the Late Pleistocene. Palaeogeography, Palaeoclimatology, Palaeoecology 680, 113317, http://doi.org/10.1016/j.palaeo.2025.113317

Li, M., Zhang, Y., Zhu, Y., Dou, H., Li, S., Xu, X., Zhou, J., Jin, Y., Cao, P., Li, Z., Wang, Z., Wang, J., Akramovich, S.A., Dong, J., 2025. The relationship between Holocene environmental evolution and human activities on the Chinese Loess Plateau inferred from an aeolian loess-paleosol profile in the Xitou Ruins. Catena 258, 109271, http://doi.org/10.1016/j.catena.2025.109271

Liu, B., Jin, H., Ge, J., Liang, X., Liang, A., Jin, J., Zhang, C., Zhao, H., Zhao, S., 2025. Quantitative analysis of the chromaticity of Holocene aeolian sand–palaeosol sequences and its application to palaeoclimate reconstruction across the Asian summer monsoonal boundary of northern China. Catena 259, 109394, http://doi.org/10.1016/j.catena.2025.109394

Wang, L., Yang, J., Gao, F., Wang, H., Zhang, C., Qu, W., Li, J., Tang, J., Liu, X., Liu, Y., Zhao, L., Wang, S., Wang, Y., Wang, F., Xia, D., 2025. Western Pacific subtropical high regulated the spatiotemporal pattern of East Asian summer monsoon precipitation during the Holocene. Palaeogeography, Palaeoclimatology, Palaeoecology 678, 113252, http://doi.org/10.1016/j.palaeo.2025.113252

Wei, X., Jiang, H., Bai, Y., Shi, W., Xu, H., Ma, X., Zhong, N., Li, S., Yin, Q., 2025. MIS 3 climate transitions revealed by high-resolution loess records from the eastern margin of the Tibetan Plateau. Palaeogeography, Palaeoclimatology, Palaeoecology 667, 112874, http://doi.org/10.1016/j.palaeo.2025.112874

Yang, S., Liu, L., Li, D., Li, R., Liu, W., Luo, Y., Li, P., Zan, J., Fang, X., 2025. New luminescence chronology of a loess-paleosol sequence at Jinchuan and its implications for aeolian deposition processes in the Tibetan Plateau. Geomorphology 478, 109730, http://doi.org/10.1016/j.geomorph.2025.109730

Zhang, W., Ding, G., Zhang, Y., Li, Y., Li, B., Lu, C., Tan, B., Sun, A., Fu, Y., An, C., 2025. Evolution of fire activity in arid Central Asia since ~12.9 ka: Transitioning from natural to anthropogenic forces. Catena 257, 109213, http://doi.org/10.1016/j.catena.2025.109213

Zhou, Y., Sun, L., Xie, Y., Kang, C., Wei, C., Wang, Y., Wei, Z., Wu, P., Liu, H., 2025. Evolution of the East Asian Summer Monsoon in the Songnen Plain, NE China since 195 ka recorded by the Harbin loess succession. Catena 259, 109343, http://doi.org/10.1016/j.catena.2025.109343

- soil

Ali, A., Achyuthan, H., Sangode, S.J., Jaiswal, M., Shah, R.A., 2025. Palaeoclimate Dynamics in Kashmir Valley: Loess Palaeosols and shifts in Mineral Magnetism during MIS 3. Journal of the Geological Society of India 101, 968-973, http://doi.org/10.17491/jgsi/2025/174193

Amrein, S., Egli, M., Duszyński, F., Migoń, P., Jancewicz, K., Tikhomirov, D., Waroszewski, J., 2025. Soil dynamics along an escarpment of a quartz sandstone tableland. Geomorphology 481, 109793, http://doi.org/10.1016/j.geomorph.2025.109793

Brandolini, F., Kinnaird, T.C., Srivastava, A., Costanzo, S., Compostella, C., Turner, S., 2025. Geoarchaeology reveals development of terrace farming in the Northern Apennines during the Medieval Climate Anomaly. Scientific Reports 15, 24989, http://doi.org/10.1038/s41598-025-08396-2

Chen, J., Zong, H., Yan, Z., Guo, Y., Zhang, D., Yang, X., He, Y., Fu, X., 2025. Age and pedogenesis of alpine grassland soils on the northeastern Qinghai-Tibetan Plateau: Insights from optical dating. Catena 258, 109217, http://doi.org/10.1016/j.catena.2025.109217

Seidel, P., Rolf, M., Holzinger, A., Gröbner, M., Riedesel, S., Laermanns, H., Feldhaar, H., Laforsch, C., Loeder, M.G.J., Bogner, C., 2025. Vertical distribution and post-depositional translocation of microplastics in a Rhine floodplain soil. Microplastics and Nanoplastics 5, 34, http://doi.org/10.1186/s43591-025-00142-9

Wang, L., Yang, J., Gao, F., Wang, H., Zhang, C., Qu, W., Li, J., Tang, J., Liu, X., Liu, Y., Zhao, L., Wang, S., Wang, Y., Wang, F., Xia, D., 2025. Western Pacific subtropical high regulated the spatiotemporal pattern of East Asian summer monsoon precipitation during the Holocene. Palaeogeography, Palaeoclimatology, Palaeoecology 678, 113252, http://doi.org/10.1016/j.palaeo.2025.113252

Zhang, A., Long, H., Yang, F., Zhang, J., Peng, J., Zhang, G., 2025. Luminescence dating illuminates soil evolution. Earth-Science Reviews 265, 105103, http://doi.org/10.1016/j.earscirev.2025.105103

- tephra (and volcanic related)

Anil, D., Devi, M., Sukumaran, P., Lakshmi, B.V., Deenadayalan, K., Kumar, S., Anoop, A., Khan, Z., Mahesh, V., Jha, G., Ajithprasad, P., Chauhan, N., 2025. Youngest Toba Tuff (YTT) beds as a Late Pleistocene isochron in the Indian subcontinent? New geochronological and sedimentological insights. Journal of Quaternary Science 40, 1176-1190, http://doi.org/10.1002/jqs.70003

Huang, C., Wang, C., Fan, A., Li, S.-H., 2025. Luminescence dating of lava-baked sediments constraints on the high frequency of Holocene eruptions in the Tengchong volcanic field, southwestern China. Science China Earth Sciences 68, 4202-4217, http://doi.org/10.1007/s11430-024-1687-1

Archaeology applications

Burnett, G., Neal, C., Reid, T., Mason, J., Doelman, T., Frolich, A., Fermor, D., Talbott, S., Mayers, W., Williams, A.N., 2025. An archaeological record of late Holocene activity and colonial impacts in the New England Tableland, New South Wales, Australia. Journal of Archaeological Science: Reports 67, 105363, http://doi.org/10.1016/j.jasrep.2025.105363

Cáceres Puro, L.M., Donaire Romero, T., Lozano Rodríguez, J.A., Díaz-Guardamino, M., Martínez-Sevilla, F., Medialdea, A., Val, M.d., Alcaina-Mateos, J., Rodríguez-Vidal, J., Muñiz Guinea, F., Vargas Jiménez, J.M., Rogerio-Candelera, M.Á., García Sanjuán, L., 2025. Seafaring megaliths: A geoarchaeological approach to the Matarrubilla giant stone basin at Valencina (Spain). Journal of Archaeological Science 180, 106263, http://doi.org/10.1016/j.jas.2025.106263

Campaña, I., Duval, M., Álvaro-Gallo, A., Guilarte, V., Shao, Q., Ortega, A.I., Arnold, L.J., Demuro, M., Bermúdez de Castro, J.M., Carbonell, E., 2025. Characterizing and dating authigenic phosphates from the sedimentary infill of Atapuerca archaeo-paleoanthropological cave sites (Spain). Quaternary Geochronology 89, 101674, http://doi.org/10.1016/j.quageo.2025.101674

Falguères, C., Gruppioni, G., Bahain, J.J., Dolo, J.M., Peresani, M., 2025. Dating the Middle Palaeolithic of Fumane Cave by the combined ESR/U-series method. Journal of Quaternary Science 40, 862-875, http://doi.org/10.1002/jqs.3719

Gkouma, M., Karkanas, P., Koukousioura, O., Syrides, G., Chalkioti, A., Tsakalos, E., Ntinou, M., Efstratiou, N., 2025. Exploring Continental and Submerged Paleolandscapes at the Pre-Neolithic Site of Ouriakos, Lemnos Island, Northeastern Aegean, Greece. Quaternary 8, 42, http://doi.org/10.3390/quat8030042

Goodman, R., Giosan, L., Shen, Z., Zimmerman, P., Lang, A., Constantinescu, S., Pizzimenti, S., Alrawi, Z., Pittman, H., 2025. The Flooding of Lagash (Iraq): Evidence for Urban Destruction Under Lugalzagesi, the King of Uruk and Umma. Geoarchaeology 40, e70027, http://doi.org/10.1002/gea.70027

Guo, X., Sun, X., Yao, Y., Yu, L., Li, F., Yi, S., Shao, K., Teng, L., Wang, Y., Zhao, C., Bae, C.J., Lu, H., 2025. Chronology of dozens of Late Paleolithic sites in the Ulan Buh Desert, northwest China. Quaternary Science Reviews 368, 109573, http://doi.org/10.1016/j.quascirev.2025.109573

Hakim, B., Wibowo, U.P., van den Bergh, G.D., Yurnaldi, D., Joannes-Boyau, R., Duli, A., Suryatman, Sardi, R., Nurani, I.A., Puspaningrum, M.R., Mahmud, I., Haris, A., Anshari, K.A., Saiful, A.M., Arman Bungaran, P., Adhityatama, S., Muhammad, P.H., Akib, A., Somba, N., Fakhri, Burhan, B., Mas'ud, Z., Moore, M.W., Perston, Y.L., Yu, W., Aubert, M., Brumm, A., 2025. Hominins on Sulawesi during the Early Pleistocene. Nature 646, 378-383, http://doi.org/10.1038/s41586-025-09348-6

Karampaglidis, T., Fenn, K., Gasparyan, B., Braucher, R., Lauer, T., Vainer, S., Gevorgyan, H., Arakelyan, D., Oikonomou, I., Haydosyan, H., Rogall, D., Carrasco, R.M., Pedraza, J., Petrosyan, A., Malinsky-Buller, A., 2025. Paleolithic hominin occupations and Quaternary geomorphological evolution in the NE Ararat Depression (Armenia). Quaternary Science Reviews 368, 109532, http://doi.org/10.1016/j.quascirev.2025.109532

Kaur, A.P., Skinner, A., Patnaik, R., 2025. Electron Spin Resonance (ESR) dating of fossil mammals from the Pinjor Formation, Upper Siwaliks, India. Quaternary International 744, 109920, http://doi.org/10.1016/j.quaint.2025.109920

Leplongeon, A., Ben Arous, E., Mesfin, I., Forestier, H., Gallet, X., Griggo, C., Puaud, S., Sémah, A.-M., Vialou, A., Pleurdeau, D., Lourdeau, A., 2025. The Last Glacial Maximum in the Tropics: Human Responses to Global Change, 30–10 ka. Journal of World Prehistory 38, 7, http://doi.org/10.1007/s10963-025-09197-1

Li, M., Zhang, Y., Zhu, Y., Dou, H., Li, S., Xu, X., Zhou, J., Jin, Y., Cao, P., Li, Z., Wang, Z., Wang, J., Akramovich, S.A., Dong, J., 2025. The relationship between Holocene environmental evolution and human activities on the Chinese Loess Plateau inferred from an aeolian loess-paleosol profile in the Xitou Ruins. Catena 258, 109271, http://doi.org/10.1016/j.catena.2025.109271

Malapaka, I., 2025. Archaeoceramic Traditions of India: Markers of Cultural Change and Continuity. International Journal of Science and Research 14, 612-616, http://doi.org/10.21275/sr25924085646

Martín-Perea, D.M., Medialdea, A., Marín, J., Abellán, N., Solano-Megías, I., Arteaga, C., Rodríguez-Hidalgo, A., Uribelarrea, D., Arroyo, X., Gidna, A., Mabulla, A., Maíllo-Fernández, J.M., 2025. Geology and chronology of the Ndutu and Naisiusiu type sites: implications for Middle and Later Stone Age occupations at Olduvai Gorge (Tanzania). Quaternary Science Reviews 368, 109578, http://doi.org/10.1016/j.quascirev.2025.109578

Medialdea, A., Damiani, S., Zeman, M., 2025. Contribution to the chronological study of the Dubrovnik Cathedral using optically stimulated luminescence. npj Heritage Science 13, 474, http://doi.org/10.1038/s40494-025-01990-7

Michalec, G., Sikora, R., Winiarska-Kabacińska, M., Odsuren, D., Wójcik, A., Moska, P., Szmit, M., Bazargur, D., Bobrowski, P., Jórdeczka, M., Szykulski, J., Muntowski, P., Gałaś, A., Gunchinsuren, B., Masojć, M., 2025. Geoarchaeological research on site formation process, paleoenvironment, and human behaviors in the early Holocene of the Gobi Desert, Mongolia. PLOS One 20, e0330209, http://doi.org/10.1371/journal.pone.0330209

Mihailović, B., Mihailović, D., Dragosavac, S., Marković, J., Pajović, D., Silva, L.O., Skinner, A., Roksandic, M., 2025. Late Middle Paleolithic and Early Upper Paleolithic of the Western Balkans: lithic assemblages from Šalitrena Pećina (Serbia). Quaternary International 749, 109990, http://doi.org/10.1016/j.quaint.2025.109990

Noghani, S., Sharifinia, A., Emami, M., Hassan Rozatian, A.S., Abdellatief, M., Khanzadi, M., 2025. Geochemical provenance studies of cultural materials from Sirvan historical Site, Ilam Province, Iran. Journal of Archaeological Science: Reports 66, 105302, http://doi.org/10.1016/j.jasrep.2025.105302

Pawlak, N.K., Chruścińska, A., Palczewski, P., Sulkowska-Tuszyńska, K., 2025. Optically stimulated luminescence dating of ancient bricks from the Church of St James in Toruń, Poland. Archaeometry 67, 1098-1117, http://doi.org/10.1111/arcm.13069

Peng, Q., Sun, M., Sun, Y., Shi, Y., Li, Y., E, C., 2025. Luminescence dating on ceramics from the Tianjun Shilin Cave around Qinghai lake in the northeastern Qinghai-Tibet plateau. Quaternary International 746, 109912, http://doi.org/10.1016/j.quaint.2025.109912

Phetkongtong, T., Klubket, P., Pailoplee, S., Limsuwan, P., Thongpool, V., 2025. Optically Stimulated Luminescence Dating of Earthenware from the Nam Tok Khao Pang Archaeological Site, Kanchanaburi, Thailand. Journal of Metals, Materials and Minerals 35, e2389, http://doi.org/10.55713/jmmm.v35i4.2389

Phetkongtong, T., Limsuwan, P., Pailoplee, S., Thongpool, V., 2025. Luminescence Dating of Brick from Nakhon Kalong City Archaeological Site in Northeastern Thailand. Suranaree Journal of Science and Technology 32, 030317, http://doi.org/10.55766/sujst9931

Saadi Ahadova, A., 2025. Radiocarbon, ESR and thermoluminescence (TL) dating of archeological monuments in Azerbaijan. Journal of Young Researcher 3, http://doi.org/10.59849/2409-4838.2025.3.126

Saktura, W.M., Jacobs, Z., Lin, S., O'Connor, S., Roberts, R.G., Malanali, W., Collins, P., 2025. Site Formation History of Widgingarri Shelter 1, Northwestern Australia and Investigation of Postdepositional Disturbance With Single-Grain OSL Dating and Soil Micromorphology. Geoarchaeology 40, e70031, http://doi.org/10.1002/gea.70031

Sanjurjo-Sánchez, J., Guasch-Ferré, N., Pitarch Martí, A., Badia, M., Menchon, J., Casas, L., Prada, J.L., 2025. New insights into the chronology of the Les Ferreres Aqueduct (Tarragona, Spain) by combining petrographic analyses and OSL dating on lime mortars. Journal of Cultural Heritage 76, 327-337, http://doi.org/10.1016/j.culher.2025.10.004

Sanjurjo-Sánchez, J., Morera Camprubí, J., Vila, O.O., 2025. First Evidence of Roman Gold Mining Obtained by Luminescence Dating of Sediments in Les Guilleteres D'All (Cerdanya, Girona, Eastern Pyrenees). Land 14, 1912, http://doi.org/10.3390/land14091912

Santi, P., Veneri, F., Tonelli, G., Tramontana, M., Panzeri, L., Galli, A., Renzulli, A., 2025. The brick material culture of Urbino (UNESCO World Heritage, Central Italy) as inferred from a multidisciplinary archaeometric study on the historic architecture. Built Heritage 9, 63, http://doi.org/10.1186/s43238-025-00233-9

Stanistreet, I.G., Stollhofen, H., Smedley, R.K., Fenn, K., Ambrose, S.H., Njau, J.K., Schick, K., Toth, N., 2025. Luminescence and radiocarbon dating the Naisiusiu Beds type section and timing of the Middle Stone Age/Later Stone Age transition at Olduvai Gorge, Tanzania. Journal of Human Evolution 207, 103675, http://doi.org/10.1016/j.jhevol.2025.103675

Teng, L., Sun, X., Liu, H., Zhao, N., Yi, S., Li, F., Guo, X., Yao, Y., Wang, Y., Bae, C.J., Lu, H., 2025. Newly discovered Late Paleolithic sites in the southeastern margin of the Badain Jaran Desert, northwest China. Quaternary Science Reviews 367, 109542, http://doi.org/10.1016/j.quascirev.2025.109542

van Beek, R., Chamberlain, E.L., de Nooijer, K., Gerritsen, S., Bartels, M., Wallinga, J., 2025. Dating earthworks with luminescence: Insights from the medieval ringfort of Den Burg, Texel (the Netherlands). Quaternary Geochronology 88, 101669, http://doi.org/10.1016/j.quageo.2025.101669

Wang, C., Shi, L., Cao, Y., Fang, L., 2025. Comparative study of luminescence dating of pottery and sediments from the Holocene Zhuqiusi site in Central China. Journal of Archaeological Science 180, 106270, http://doi.org/10.1016/j.jas.2025.106270

Wang, J., Tan, P., Feng, Y., Zheng, Z., Guo, Y., He, J., Wang, Y., Zhang, J., 2025. Human presence in the southeastern Tibetan Plateau after the Last Glacial Maximum. Palaeogeography, Palaeoclimatology, Palaeoecology 667, 112878, http://doi.org/10.1016/j.palaeo.2025.112878

Way, A.M., Nejman, L., Hughes, P., Lisá, L., Wright, D., Nývltová Fišáková, M., Sullivan, M., Moska, P., Spooner, N.A., Škrdla, P., Mlejnek, O., Skopal, N., Neruda, P., Nerudová, Z., Přichystal, A., Králík, M., Sůvová, Z., 2025. Re-excavation of cultural deposits at Švédův stůl cave in the Moravian Karst, Czech Republic. Journal of Archaeological Science: Reports 67, 105449, http://doi.org/10.1016/j.jasrep.2025.105449

Wei, J., Jin, J., Ling, Z., Zhang, W., Wei, C., Zuo, X., Li, Z., Hou, C., Xu, D., 2025. Chronological sequencing, site selection, and environmental context of Neolithic island settlements in southeastern coastal China. Quaternary International 748, 109978, http://doi.org/10.1016/j.quaint.2025.109978

Westell, C., Roberts, A., Morley, M.W., Moffat, I., Hernandez, V.C., Spooner, N.A., McDonnell, K., Rudd, R., Petchey, F., 2025. Life beyond the lakes: An analysis and implications of a Pleistocene combustion feature on the Pike River in South Australia. Journal of Archaeological Science 180, 106264, http://doi.org/10.1016/j.jas.2025.106264

Yu, W., Herries, A.I.R., Joannes-Boyau, R., 2025. The challenges of direct dating of fossil teeth from the Australopithecus africanus, Taung Child type site, South Africa. Quaternary Geochronology 90, 101696, http://doi.org/10.1016/j.quageo.2025.101696

ESR, basic and applied research

Campaña, I., Duval, M., Álvaro-Gallo, A., Guilarte, V., Shao, Q., Ortega, A.I., Arnold, L.J., Demuro, M., Bermúdez de Castro, J.M., Carbonell, E., 2025. Characterizing and dating authigenic phosphates from the sedimentary infill of Atapuerca archaeo-paleoanthropological cave sites (Spain). Quaternary Geochronology 89, 101674, http://doi.org/10.1016/j.quageo.2025.101674

Falguères, C., Gruppioni, G., Bahain, J.J., Dolo, J.M., Peresani, M., 2025. Dating the Middle Palaeolithic of Fumane Cave by the combined ESR/U-series method. Journal of Quaternary Science 40, 862-875, http://doi.org/10.1002/jqs.3719

Hakim, B., Wibowo, U.P., van den Bergh, G.D., Yurnaldi, D., Joannes-Boyau, R., Duli, A., Suryatman, Sardi, R., Nurani, I.A., Puspaningrum, M.R., Mahmud, I., Haris, A., Anshari, K.A., Saiful, A.M., Arman Bungaran, P., Adhityatama, S., Muhammad, P.H., Akib, A., Somba, N., Fakhri, Burhan, B., Mas'ud, Z., Moore, M.W., Perston, Y.L., Yu, W., Aubert, M., Brumm, A., 2025. Hominins on Sulawesi during the Early Pleistocene. Nature 646, 378-383, http://doi.org/10.1038/s41586-025-09348-6

Kaur, A.P., Skinner, A., Patnaik, R., 2025. Electron Spin Resonance (ESR) dating of fossil mammals from the Pinjor Formation, Upper Siwaliks, India. Quaternary International 744, 109920, http://doi.org/10.1016/j.quaint.2025.109920

Mihailović, B., Mihailović, D., Dragosavac, S., Marković, J., Pajović, D., Silva, L.O., Skinner, A., Roksandic, M., 2025. Late Middle Paleolithic and Early Upper Paleolithic of the Western Balkans: lithic assemblages from Šalitrena Pećina (Serbia). Quaternary International 749, 109990, http://doi.org/10.1016/j.quaint.2025.109990

Mothé, D., Kinoshita, A., Baffa, O., Luna, C.A., 2025. Doing the time warp again: Electron Spin Resonance dating reveals oldest numeric age for Notiomastodon platensis Ameghino, 1888 (Mammalia, Proboscidea). Geobios 91, 81-88, http://doi.org/10.1016/j.geobios.2024.11.008

Prince, E., Tsukamoto, S., Grützner, C., Bülhoff, M., Ustaszewski, K., 2025. Deciphering Pleistocene Fault Activity in the Eastern Alps: Dating Fault Gouges With Electron Spin Resonance and Optically Stimulated Luminescence. Tectonics 44, 008662, http://doi.org/10.1029/2024tc008662

Saadi Ahadova, A., 2025. Radiocarbon, ESR and thermoluminescence (TL) dating of archeological monuments in Azerbaijan. Journal of Young Researcher 3, http://doi.org/10.59849/2409-4838.2025.3.126

Song, H., Liang, Z., Duan, M., Liu, M., Liu, L., Chen, Z., Han, S., Zhang, H., Zhou, C., 2025. Quaternary stratigraphy of Bayan borehole in eastern Songnen Plain and its paleoclimate significance. Scientific Reports 15, 32027, http://doi.org/10.1038/s41598-025-15418-6

Xin, C., Yan, S., Li, H., Dai, X., Liu, T., Wang, J., 2025. Cenozoic Multiphasic Activity and Mesozoic Basin-Control Role of the Dingri–Gangba Fault, Southern Tibet: An Integrated Study of Structural Analysis,

Stratigraphic Correlation, and ESR Geochronology. Geosciences 15, 440, http://doi.org/10.3390/geosciences15110440

Yu, W., Herries, A.I.R., Joannes-Boyau, R., 2025. The challenges of direct dating of fossil teeth from the Australopithecus africanus, Taung Child type site, South Africa. Quaternary Geochronology 90, 101696, http://doi.org/10.1016/j.quageo.2025.101696

Zhang, J., Tsukamoto, S., 2025. R scripts for dose rate calculation in trapped charge dating. Ancient TL 43, 20-28, http://doi.org/10.26034/la.atl.2025.7701

Zhang, X., Ai, C., Kong, F., Zhao, J., Gong, Y., Pei, Y., He, J., 2025. Sediment Transport into the Saline Western Songnen Basin of NE China from the Late Early Pleistocene to the Early Holocene. Land 14, 2263, http://doi.org/10.3390/land14112263

Zhou, Y., Sun, L., Xie, Y., Kang, C., Wei, C., Wang, Y., Wei, Z., Wu, P., Liu, H., 2025. Evolution of the East Asian Summer Monsoon in the Songnen Plain, NE China since 195 ka recorded by the Harbin loess succession. Catena 259, 109343, http://doi.org/10.1016/j.catena.2025.109343

Basic research

Amorim, Y.F., Nunes, M.C.S., Chruścińska, A., Wiśniewski, K., Trindade, N.M., 2025. First LM-OSL analysis of natural alexandrite. Radiation Measurements 184, 107441, http://doi.org/10.1016/j.radmeas.2025.107441

Amrein, S., Egli, M., Duszyński, F., Migoń, P., Jancewicz, K., Tikhomirov, D., Waroszewski, J., 2025. Soil dynamics along an escarpment of a quartz sandstone tableland. Geomorphology 481, 109793, http://doi.org/10.1016/j.geomorph.2025.109793

Ataee, N., Roberts, H.M., Duller, G.A.T., 2025. Assessing the potential of a modified post-isothermal IRSL (pIt-IR) protocol to circumvent the problems posed by anomalous fading in polymineral fine grains. Quaternary Geochronology 88, 101676, http://doi.org/10.1016/j.quageo.2025.101676

Gong, Z., Yan, H., Luo, M., 2025. Study the effect of irradiation, optical bleaching and heating on the thermal stability of OSL signals of quartz from dune sands in northern China. Quaternary Geochronology 88, 101672, http://doi.org/10.1016/j.quageo.2025.101672

Hou, C., Jin, J., Ma, M., Liu, G., Ling, Z., Wei, J., Xu, D., 2025. Temporal variation of luminescence sensitivity and environmental changes during the mid-late Holocene recorded in estuarine coastal deposits from South China. Catena 255, 109022, http://doi.org/10.1016/j.catena.2025.109022

Kitis, G., Polymeris, G.S., Peng, J., 2025. Determining equivalent dose for optically stimulated luminescence (OSL) dating with physically meaningful dose response curves. Quaternary Geochronology 88, 101671, http://doi.org/10.1016/j.quageo.2025.101671

Lukas, E., Santos, A.M.C., Ganija, M., Veitch, P., 2025. Evaluating the effects of increased stimulation power on a beryllium oxide real-time optically stimulated luminescence fibre-coupled dosimeter. Radiation Measurements 184, 107439, http://doi.org/10.1016/j.radmeas.2025.107439

Majgier, R., Maternicki, K., Mandowski, A., Moska, P., Biernacka, M., Kreutzer, S., 2025. The Helios OSL reader: a portable system for dating and dosimetry applications. Geochronometria 52, 208873, http://doi.org/10.20858/geochr/208873

Marngar, A., Dubey, V., 2025. Thermoluminescence (TL) properties of quartz from different geological settings and their implications for geological dating and radiation dosimetry. Journal of Radioanalytical and Nuclear Chemistry 334, 7599-7621, http://doi.org/10.1007/s10967-025-10464-w

Maßon, L.A.E., Riedesel, S., Opitz, S., Zander, A., Bell, A., Cieszynski, H., Reimann, T., 2025. How much K is OK? Evaluating different methods for K-concentration determination and the effect of the internal K concentration on feldspar luminescence dating. Geochronology 7, 475-492, http://doi.org/10.5194/gchron-7-475-2025

Singhal, M., Moitra, H., Mitra, S., Panda, A., Yadav, J.K., Sarma, D.S., Kumar, D., Chauhan, N., Gupta, S., Singhvi, A.K., 2025. Luminescence characteristics of terrestrial Jarosite from Kachchh, India: A Martian analogue. Meteoritics & Planetary Science 60, 1921-1938, http://doi.org/10.1111/maps.70021

Sontag-González, M., Murari, M.K., Jain, M., Frouin, M., Fuchs, M., 2025. Further investigations into the accuracy of infrared radiofluorescence (IR-RF) and its inter-comparison with infrared photoluminescence (IRPL) dating. Geochronology 7, 289-308, http://doi.org/10.5194/gchron-7-289-2025

Xu, S., Rui, X., Guo, Y., Li, B., 2025. Testing micro-aliquot SGC and LnTn methods for age determination up to 780 ka using coarse K-feldspar grains from Nihewan Basin, northern China. Quaternary Geochronology 88, 101673, http://doi.org/10.1016/j.quageo.2025.101673

Dosimetry

Ekendahl, D., Čemusová, Z., Sofer, Z., Plutnarová, I., 2025. Thermoluminescence and optically stimulated luminescence dosimetry with NaCl detectors made at different sintering temperatures. Radiation Measurements 184, 107443, http://doi.org/10.1016/j.radmeas.2025.107443

Kreutzer, S., Martin, L., Miallier, D., Mercier, N., 2025. Environmental gamma dose rate measurements using cadmium zinc telluride (CZT) detectors. Geochronology 7, 229-246, http://doi.org/10.5194/gchron-7-229-2025

Maßon, L.A.E., Riedesel, S., Opitz, S., Zander, A., Bell, A., Cieszynski, H., Reimann, T., 2025. How much K is OK? Evaluating different methods for K-concentration determination and the effect of the internal K concentration on feldspar luminescence dating. Geochronology 7, 475-492, http://doi.org/10.5194/gchron-7-475-2025

Silva, C.R.E., Meira-Belo, L.C., 2025. Implementation of retrospective dosimetry using ceramic material from spark plugs. Applied Radiation and Isotopes 225, 112067, http://doi.org/10.1016/j.apradiso.2025.112067

Toktamis, H., Güneş, Tamer S., Toktamis, D., 2025. Investigation of the Use of Naturally Grown $CaCO_3$ Crystals on Rocks as a Radiation Dosimeter via Thermoluminescence Method. Luminescence 40, e70217, http://doi.org/10.1002/bio.70217

Zhang, J., Tsukamoto, S., 2025. R scripts for dose rate calculation in trapped charge dating. Ancient TL 43, 20-28, http://doi.org/10.26034/la.atl.2025.7701

Minerals other than quartz and feldspar

Ekendahl, D., Čemusová, Z., Sofer, Z., Plutnarová, I., 2025. Thermoluminescence and optically stimulated luminescence dosimetry with NaCl detectors made at different sintering temperatures. Radiation Measurements 184, http://doi.org/10.1016/j.radmeas.2025.107443

Toktamis, H., Güneş, Tamer S., Toktamis, D., 2025. Investigation of the Use of Naturally Grown $CaCO_3$ Crystals on Rocks as a Radiation Dosimeter via Thermoluminescence Method. Luminescence 40, http://doi.org/10.1002/bio.70217

Portable instruments

Majgier, R., Maternicki, K., Mandowski, A., Moska, P., Biernacka, M., Kreutzer, S., 2025. The Helios OSL reader: a portable system for dating and dosimetry applications. Geochronometria 52, e208873, http://doi.org/10.20858/geochr/208873

Smedley, R., Pannozzo, N., Boyle, J., Clarke, D., Lario, J., Plater, A., 2025. Portable luminescence for rapidly identifying tsunami dynamics and responses in saltmarshes. Science of the Total Environment 1002, 180548, http://doi.org/10.1016/j.scitotenv.2025.180548

Review

Leplongeon, A., Ben Arous, E., Mesfin, I., Forestier, H., Gallet, X., Griggo, C., Puaud, S., Sémah, A.-M., Vialou, A., Pleurdeau, D., Lourdeau, A., 2025. The Last Glacial Maximum in the Tropics: Human Responses to Global Change, 30–10 ka. Journal of World Prehistory 38, 7, http://doi.org/10.1007/s10963-025-09197-1

McKeever, S.W.S., 2025. Glow curve deconvolution – Why are most published results wrong? Common pitfalls in measurement and analysis. Radiation Measurements 189, 107537, https://doi.org/10.1016/j.radmeas.2025.107537

Riedesel, S., 2025. Not fade away - The persistence of fading in feldspar luminescence. Ancient TL 43, 9-19, https://doi.org/10.26034/la.atl.2025.7620

Zhang, A., Long, H., Yang, F., Zhang, J., Peng, J., Zhang, G., 2025. Luminescence dating illuminates soil evolution. Earth-Science Reviews 265, 105103, http://doi.org/10.1016/j.earscirev.2025.105103

Statistics, simulation, and modelling

Kitis, G., Polymeris, G.S., Peng, J., 2025. Determining equivalent dose for optically stimulated luminescence (OSL) dating with physically meaningful dose response curves. Quaternary Geochronology 88, http://doi.org/10.1016/j.quageo.2025.101671

Lukas, E., Santos, A.M.C., Ganija, M., Veitch, P., 2025. Evaluating the effects of increased stimulation power on a beryllium oxide real-time optically stimulated luminescence fibre-coupled dosimeter. Radiation Measurements 184, 107439, http://doi.org/10.1016/j.radmeas.2025.107439

Xu, S., Rui, X., Guo, Y., Li, B., 2025. Testing micro-aliquot SGC and LnTn methods for age determination up to 780 ka using coarse K-feldspar grains from Nihewan Basin, northern China. Quaternary Geochronology 88, 101673, http://doi.org/10.1016/j.quageo.2025.101673

Yüksel, M., Deniz, F., Ünsal, E., 2025. ANN-Based Prediction of OSL Decay Curves in Quartz from Turkish Mediterranean Beach Sand. Crystals 15, 733, http://doi.org/10.3390/cryst15080733

Conference Announcements: LED 2026

18th International Conference on Luminescence and Electron Spin Resonance Dating (LED 2026)

6th-10th September 2026.

SESAME (Synchrotron-light for Experimental Science and Applications in the Middle East), is inviting you to participate in the 18th International Conference on Luminescence and Electron Spin Resonance Dating (LED 2026).

The conference will take place at the Landmark Amman Hotel, Amman, Jordan (landmarkamman.com) between 6th and 10th September 2026.

The conference will be followed by an optional 2-day (11th-12th September 2026) archaeological field trip that will bring the participants to Petra and Wadi Rum.

The conference aims to foster a meaningful academic exchange, and bring together students, early-career scholars, and experienced researchers from around the world.

The research areas for conference presentations will cover the topics

- Basic physical processes
- Advances in methodology for equivalent dose estimation
- Advances in dose rate determination
- Instrumentation
- Applications in geosciences
- Applications in archaeology
- Modelling
- New applications

For further information about registration, abstract submission, visit our website for more information and updates:
https://indico.sesame.org.jo/e/led2026

The website will be regularly updated.

Ancient TL

ISSN 2693-0935

Aims and Scope

Ancient TL (electronic ISSN 2693-0935) is a community-based, not-for-profit, peer-reviewed, diamond open access journal devoted to theoretical and experimental luminescence and electron spin resonance (ESR) research. This includes research on environmental dose rate, rock thermal histories (e.g., low-temperature thermochronometry) and mineral provenance and characterisation. Manuscripts on luminescence and ESR dating, on software codes, numerical models and on instrumentation are also welcome. Ancient TL also publishes interlaboratory comparisons, standardisation procedures, failed experiments, as well as observations difficult to explain. Following Ancient TL's tradition, manuscripts about practical aspects of laboratory and field work are explicitly welcome. Periodically, Ancient TL publishes an up-to-date bibliography, thesis abstracts, and miscellaneous information for the community.

Frequency

Two issues per annum in June and December

Submission of articles to Ancient TL

For instructions to authors and information on how to submit to Ancient TL, please visit the website at:
http://ancienttl.org/TOC1.htm

Journal Enquiries

For enquiries please contact the editor:
Christoph Schmidt, Institute of Earth Surface Dynamics, University of Lausanne, 1015 Lausanne, Switzerland, Tel: +41-21-692-3516 (christoph.schmidt@unil.ch)

Subscriptions to Ancient TL

Ancient TL Vol. 32, No. 2 December 2014 was the last issue to be published in print. Past and current issues are available for download free of charge from the Ancient TL website:
http://ancienttl.org/TOC4.htm